

# The properties of the young stellar populations in powerful radio galaxies at low and intermediate redshifts

J. Holt<sup>1\*</sup>, C. N. Tadhunter<sup>1</sup>, R. M. González Delgado<sup>2</sup>, K. J. Inskip<sup>1</sup>, J. Rodríguez<sup>1</sup>,  
B. H. C. Emonts<sup>3</sup>, R. Morganti<sup>4</sup>, K. A. Wills<sup>1</sup>,

<sup>1</sup>*Department of Physics and Astronomy, University of Sheffield, Sheffield, S3 7RH, UK.*

<sup>2</sup>*Instituto de Astrofísica de Andalucía (CIASC), Apdo. 3004, 18080 Granada, Spain.*

<sup>3</sup>*Kapteyn Astronomical Institute, University of Groningen, P. O. Box 800, 9700 AV Groningen, The Netherlands.*

<sup>4</sup>*Netherlands Foundation for Research in Astronomy, Postbus 2, 7990 AA Dwingeloo, The Netherlands*

18 October 2021

## ABSTRACT

We present high-quality, wide spectral coverage long-slit optical spectra for 12 powerful radio sources at low and intermediate redshifts ( $z < 0.7$ ) that show evidence for a substantial UV excess. These data were taken using the WHT and VLT telescopes with the aim of determining the detailed properties of the young stellar populations (YSPs) in the host galaxies as part of a larger project to investigate evolutionary scenarios for the AGN host galaxies. The results of our spectral synthesis model fits to the spectra highlight the importance of taking into account AGN-related components (emission lines, nebular continuum, scattered light) and reddening of the stellar populations in studies of this type. It is also clear that careful examination of the fits to the spectra, as well as consideration of auxiliary polarimetric and imaging data, are required to avoid degeneracies in the model solutions. In 3 out of the 12 sources in our sample we find evidence for broad permitted line components, and a combination of AGN-related continuum components and an old (12.5 Gyr) stellar population provides an adequate fit to the data. However, for the remaining 9 sources we find strong evidence for YSPs. In contrast to some recent studies that suggest relatively old post-starburst ages for the YSPs in radio galaxies (0.3 – 2.5 Gyr), we deduce a wide range of ages for the YSPs in our sample objects (0.02 – 1.5 Gyr), with  $\sim 50\%$  of the sample showing evidence for young YSP ages ( $\lesssim 0.1$  Gyr) in their nuclear regions. The nuclear YSPs are often significantly reddened ( $0.2 < E(B - V) < 1.4$ ) and make up a substantial fraction ( $\sim 1 - 35\%$ ) of the total stellar mass in the regions sampled by the spectroscopic slits. Moreover, in all the cases in which we have sufficient spatial resolution we find that the UV excess is extended across the full measureable extent of the galaxy (typically 5 – 30 kpc), suggesting galaxy-wide starbursts. The implications for photometric and spectroscopic studies of active galaxies are discussed.

**Key words:** galaxies: active, galaxies: radio galaxies, galaxies: starburst, galaxies: stellar content

## 1 INTRODUCTION

Major merger events are often invoked to explain the origin of nuclear activity in galaxies. Indeed, there is much observational evidence to suggest that, in a significant fraction of the local radio source population, the activity has been triggered by merger events involving two or more galaxies where at least one is gas rich. Despite the fact that the overwhelming majority of radio galaxies are classified

as elliptical or S0 types, deep optical imaging studies reveal double nuclei, tidal tails, arcs of emission and distorted isophotes characteristic of mergers in  $\sim 50\%$  of nearby radio galaxies with strong emission lines (Heckman et al. 1986; Smith & Heckman 1989). In addition, kinematical studies of the emission line gas (e.g. Tadhunter et al. 1989; Baum et al. 1992) further support the idea that the early-type hosts are interacting and/or merging with companion galaxies. However, there is a limit to what can be deduced from the imaging and kinematical studies alone, especially in terms of gauging the type of merger (major or minor? dry

\* E-mail: j.holt@sheffield.ac.uk

or gas-rich?), the order of events in the triggering of the activity, and the relationship between radio galaxies and other types of merging systems such as ultraluminous infrared galaxies (ULIRG).

Given that gas-rich mergers can also trigger starbursts, studies of the stellar populations in the early-type host galaxies of radio sources have the potential to provide key information about the natures and timescales of the triggering events. A major challenge in such studies is to identify the young stellar populations in the presence of activity-related components such as nebular continuum, direct or scattered AGN light and emission lines, all of which are likely to be significant in galaxies hosting powerful, quasar-like AGN (Tadhunter et al. 2002). Therefore, although the broad-band colours of many radio galaxies show UV excesses compared to normal, passively evolving elliptical galaxies (Lilly & Longair 1984; Smith & Heckman 1989), such excesses may be related more to the AGN activity than any merger induced star formation. Nonetheless, by taking particular care to account for all the activity related components, it has proved possible to use spectral synthesis modelling techniques to reveal the presence of young stellar populations (YSPs) in radio galaxies (e.g. Tadhunter et al. 1996). In this way Tadhunter et al. (2002) found evidence for YSPs in 30 – 50% of a complete sample of southern 2Jy radio galaxies at intermediate redshifts, Wills et al. (2002) deduced the presence of YSPs in 30% of their complete sample of nearby 3C radio galaxies with FR II radio morphologies, and Wills et al. (2004) detected YSPs in 25% of a small sample of lower radio power FR I radio sources from the 2Jy sample. More recently, Raimann et al. (2005) found a higher rate of incidence of YSPs in a sample of 20 nearby radio galaxies ( $\sim 100\%$ ). However, the latter authors did not explicitly account for all the AGN-related continuum and emission line components, and assumed a priori that the optical spectra of their radio galaxies could be modelled in terms of 5 stellar components of varying age.

Although all the previous studies revealed the presence of young stellar populations in a significant fraction of radio galaxy hosts, the data were not always of sufficiently high quality in terms of spectral range, spectral resolution and S/N to allow the detailed properties of the YSPs to be deduced, and thereby learn about the nature of the triggering merger events. We have therefore begun a major programme to obtain the requisite data and investigate the stellar populations in all nearby radio galaxies already suspected of having YSPs on the basis of previous work, aiming to analyse the data for all the objects in a uniform way. Some early results from this programme for 5 nearby radio galaxies were presented in Tadhunter et al. (2005); Emonts et al. (2006) and Holt et al. (2006). The latter papers also give a full account of the background to the project. In this paper we present the results for a further 12 radio galaxies at low and intermediate redshifts ( $z < 0.7$ )<sup>1</sup>, extending detailed studies of the YSPs in radio galaxies up to higher redshifts than the previously published work. The implications of the results of the programme as a whole for our understanding of the evolution of the host galaxies, triggering of the activity and the heating of the far-IR emitting dust in AGN are discussed

in separate papers (Tadhunter et al. 2007, Tadhunter et al. in prep).

## 2 THE SAMPLE

The sample considered in this paper comprises 12 powerful low and intermediate redshift ( $z < 0.7$ ) radio galaxies. All have been selected on the basis of having a strong UV excess that is difficult to explain solely in terms of AGN-related components (see the discussion in Tadhunter et al. 2002). In essence, all sources in this sample are suspected of having a large contribution of continuum light from a young stellar population (YSP). Therefore they are suitable for detailed studies of the young stellar populations.

The sample spans both the northern and southern skies. The northern objects originate from the 3C catalogue whilst the southern objects derive from the well-studied 2Jy sample of radio galaxies (e.g. Tadhunter et al. 1993; Morganti et al. 1993; Tadhunter et al. 2002). Table 1 lists the properties of the sample.

Although many of the objects in our sample have been previously modelled (Tadhunter et al. 1996; Aretxaga et al. 2001; Robinson 2001; Wills et al. 2002, 2004; Raimann et al. 2005), for most we have new data with improved spectral resolution, spectral coverage and S/N. We also fit these data with the newer, higher resolution spectral synthesis models of Bruzual & Charlot (2003), taking full account of reddening of the YSPs and potential AGN contributions to the optical/UV continuum.

## 3 OBSERVATIONS AND DATA REDUCTION

The northern sample was observed using the ISIS dual-beam spectrograph on the William Herschel Telescope (WHT) on La Palma in several runs between 1996 and 2005. The southern sample was observed during a single run in 2003 using the FORS2 spectrograph on the ESO Very Large Telescope (VLT) on Cerro Paranal, Chile. Table 2 summarises the observations and the various instrumental setups. Note that, in the case of the highest redshift source in our sample (also the faintest) — PKS 0409-75 — we nodded the source along the slit in order to improve the sky subtraction at the red end of the spectrum. Although for 3C 321 we use the same data set as that used in Robinson et al. (2000), for this paper, we have improved the flux calibration and re-modelled the SEDs using the latest models, for the first time taking into account reddening of the YSP.

This project focusses on accurate modelling of the (often faint) continuum emission. Hence, all observations were made with a 1.3-1.5 arcsec slit in order to include as much of the light from the galaxy as possible, whilst retaining sufficient wavelength resolution to allow detection and modelling of stellar absorption features. To reduce the effects of differential refraction, all exposures were taken at low airmass (sec  $z < 1.1$ ), with the slit aligned along the parallactic angle, and/or (in the case of the VLT observations) using a linear atmospheric dispersion compensator (LADC) that was reset between exposures. The slit PAs are listed in Table 2 (for reference, the radio axis PAs are presented in Table 1).

<sup>1</sup>  $H_0 = 75 \text{ km s}^{-1} \text{ Mpc}^{-1}$ ,  $q_0 = 0.0$  assumed throughout.

**Table 1.** Properties of the sample. (a) radio source; (b) redshift; (c) Galactic reddening from Schlegel et al. (1998) (E(B-V)); (d) radio luminosity at 5GHz calculated from the flux densities in Wall & Peacock (1985) except 3C 285 (from Kellerman et al. 1969); (e) radio spectral index for  $\alpha_{2.7\text{GHz}}^{5\text{GHz}}$  where  $F_\nu \propto \nu^{-\alpha}$ , (f) radio morphology and (g) optical spectral classification (see text for references).

**redshifts:** \* Holt (2005); † van Breugel & Dey (1993); ◊ de Grijp et al. (1992); ◊ Hill et al. (1996); ▷ Smith et al. (2004); \* Tadhunter et al. (1993); ◁ de Vaucouleurs et al. (1991). References to the other data can be found in the text.

(a)	(b)	(c)	(d)	(e)	(f)	(g)
3C 218	0.05488▷	0.042	25.91	0.9	FRI/FRII, symmetric	NLRG
3C 236	0.101◊	0.011	25.44	0.7	FRII, double-double	NLRG
3C 285	0.079†	0.017	25.00	1.27	FRII	NLRG
3C 321	0.096◊	0.044	25.33	1.14	FRII	NLRG
3C 381	0.161‡	0.053	25.87	0.96	FRII	BLRG
3C 433	0.106‡	0.044	25.94	1.07	FRI/FRII, x-shaped	NLRG
PKS 0023-26	0.322*	0.014	27.33	0.7	CSS	NLRG
PKS 0039-44	0.346*	0.007	26.57	0.93	FRII	NLRG
PKS 0409-75	0.693*	0.078	27.82	0.86	FRII	NLRG
PKS 1932-46	0.231*	0.054	26.65	1.03	FRII	BLRG
PKS 2135-209	0.636*	0.033	27.47	0.82	CSS	BLRG
NGC 612	0.030◁	0.020	24.85	0.51	FRI/FRII, 'hybrid'	NLRG

### 3.1 Data reduction

The data were reduced in the usual way (bias subtraction, flat fielding, cosmic ray removal, wavelength calibration, flux calibration) using the standard packages in IRAF. The two-dimensional spectra were also corrected for spatial distortions of the CCD. The final wavelength calibration accuracies, calculated using the standard error on the mean deviation of the night sky emission line wavelengths from published values (Osterbrock et al. 1996), ranged between 0.05-0.5Å. The spectral resolution, calculated using the widths of the night sky emission lines, ranged between 4-10Å. Both are dependent on the instrumental setup and the wavelength range observed.

Comparison of several spectrophotometric standard stars observed with a wide slit (5 arcsec) throughout each run gave relative flux calibrations accurate to  $\pm 5$  per cent. This accuracy was confirmed by good matching in the flux between the red and blue spectra. For the VLT observations, and for 3C 236, further observations of standard stars close in position and time to each target observation with a narrow slit, matched to the slit width used to observe the objects, were used to correct for atmospheric absorption features (e.g. A and B bands at  $\sim 7600$  and  $\sim 6800$  Å respectively). The spectra of all sources were corrected for Galactic extinction using the E(B-V) values from Schlegel et al. (1998) and the Seaton (1979) extinction law.

The spectra were extracted and analysed using the STARLINK packages FIGARO and DIPSO, and CONFIT, a customised IDL minimum  $\chi^2$  fitting programme (Robinson 2001; Tadhunter et al. 2005).

## 4 RESULTS

The continuum spectra for all sources were analysed using three main steps: first, the degree of the UV excess and its spatial distribution were assessed using the 4000Å break; second, the overall spectral energy distribution (SED) shape was modelled using a combination of nebular, stellar and power-law continua (which could represent an AGN-like or very young stellar population continuum); and finally, making detailed comparisons between the better fitting SED models and the data using stellar absorption lines (e.g. Balmer lines, CaII K). The individual steps are described in detail below.

### 4.1 The 4000Å break

A simple, commonly used diagnostic tool for investigating the magnitude of the UV excess in a galaxy spectrum is to compare the continuum flux on either side of the 4000Å break (e.g. Tadhunter et al. 2002, 2005). Hence, for each galaxy, continuum slices on either side of 4000Å were extracted to estimate the  $D(4000)$  ratio – a measure of the 4000Å break amplitude – following the definition in Tadhunter et al. (2002, 2005):

$$D(4000) = \frac{\int_{4150}^{4250} F_\lambda d\lambda}{\int_{3750}^{3850} F_\lambda d\lambda} \quad (1)$$

This form of the  $D4000$  ratio is better suited to active galaxies than the original form (see e.g. Bruzual & Charlot 1993) as it is not contaminated by bright emission lines (e.g. [Ne III]λ3869). The  $D(4000)$  ratio is also insensitive to both

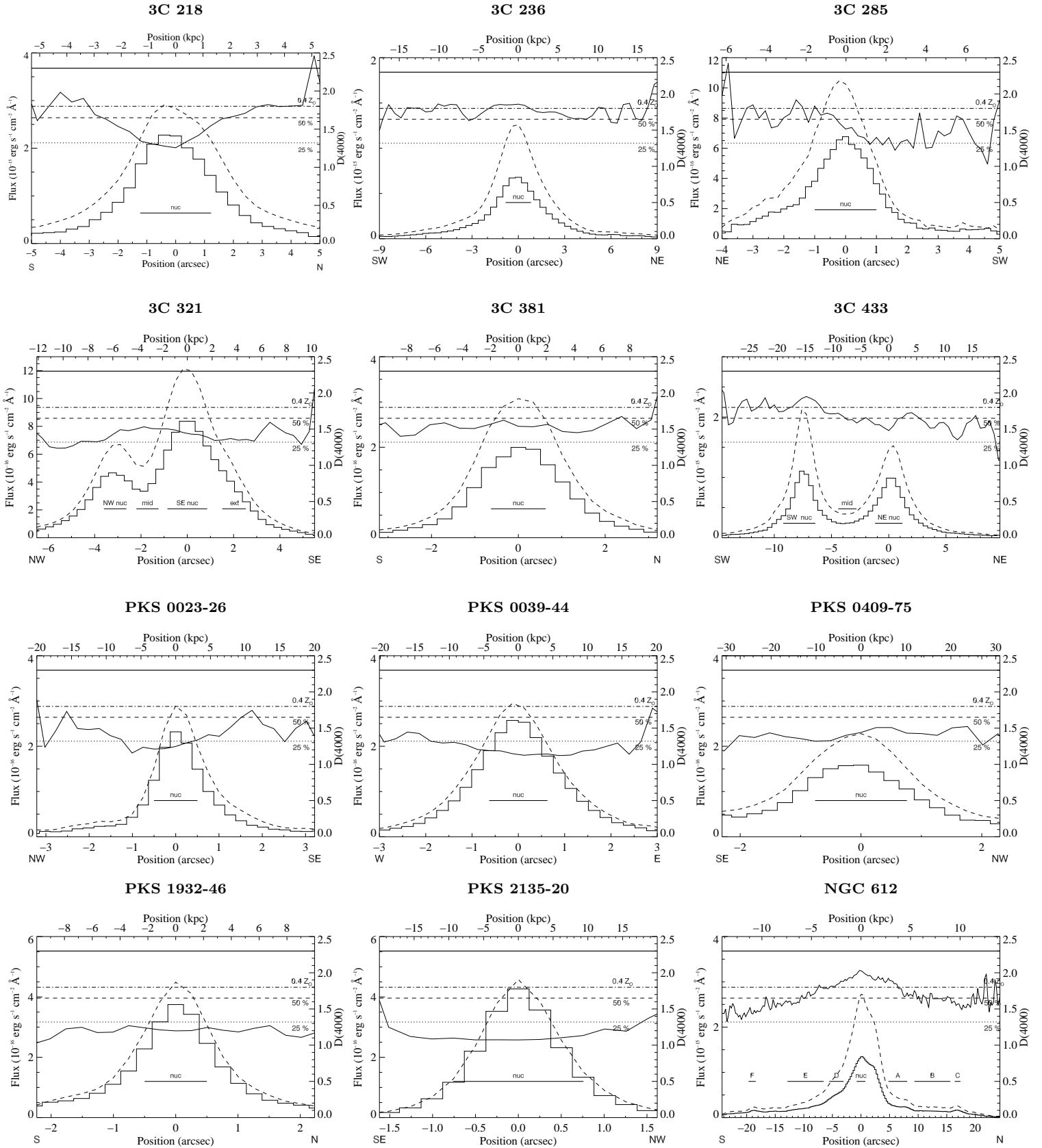


**Figure 1.**  $D(4000)$  ratio for all galaxies in the sample. The solid and dashed lines (profiles) represent the integrated continuum flux in the ranges 3750-3850 Å and 4150-4250 Å respectively. The  $D(4000)$  ratio is overlotted (faint solid line) along with the expected ratios for a pure 12.5 Gyr elliptical galaxy (bold solid horizontal line) and dotted with a 50 per cent featureless continuum in the 3800 Å bin (dashed horizontal line) and with a 75 per cent featureless continuum (dotted horizontal line). The ratio expected for a subsolar metallicity ( $Z = 0.4 Z_{\odot}$ ) 12.5 Gyr population is also shown (dot-dashed horizontal line). The locations of all apertures used in the analysis are also marked.

**Table 2.** Summary of the observations. Note, the wavelength ranges given are the *useful* wavelength ranges of the spectra. Further, where the end/start wavelengths of the blue/red frames are equal, these are where the ‘trim’ was made for the fitting – in the majority of sources there was considerable overlap between the blue and red frames, of order a few hundred angstroms.

Date	Object	Setup (arm/CCD/grating/filter)	Exposure (s)	Slit		Rest $\lambda$ range (Å)	Seeing (arcsec)
				PA (°)	width (arcsec)		
<b>WHT/ISIS</b>							
13/01/2004	3C 218	B/EEV12/R300B/-	3*1200	10	1.27	3000-5950	~1
		R/MARCONI2/R316R/GG495	3*1200	10	1.27	5950-8000	~1
12/05/2001	3C 236	B/EEV12/R300B/-	2*1200	50	1.3	3040-5640	0.7
		R/TEK4/R316R/GG495	2*1200	50	1.3	5640-6880	0.7
06/06/2005	3C 285	B/EEV12/R300B/-	3*1200	209	1.23	3100-4848	0.6
		R/MARCONI2/R316R/-	3*1200	209	1.23	4848-6994	0.6
22/07/1996	3C 321	B/LORAL1/R158B/-	2*1500	130	1.37	3309-5700	<1.0
		R/TEK5/R158R/GG495	2*1500	130	1.37	5883-8100	<1.0
22/07/1996	3C 381	B/LORAL1/R158B/-	2*900	20	1.34	3123-5560	0.8-1.0
		R/TEK5/R158R/GG495	1*900,1*1300	20	1.34	5560-8464	0.8-1.0
31/07/2005	3C 433	B/EEV12/R300B/-	3*1200	32	1.54	2800-4900	1.1-1.7
		R/MARCONI2/R316R/GG495	3*1200	32	1.54	4900-7433	1.1-1.7
<b>VLT/FORS2</b>							
24/09/2003	PKS 0023-26	B/MIT/G600B/-	3*1000	145	1.3	2850-3800	0.7-0.8
		R/MIT/G600RI/GG435+81	3*1000	145	1.3	3800-6100	0.7-0.8
25/09/2003	PKS 0039-44	B/MIT/G600B/-	3*1000	72	1.3	2900-4200	0.7-1.0
		R/MIT/G600RI/GG435+81	3*1000	72	1.3	4200-6132	0.7-1.0
24/09/2003	PKS 0409-75	R/MIT/G600RI/GG435+81	12*600	-30	1.3	2921-4875	1.0-1.2
		R/MIT/G600Z/OG590+32	6*600	-30	1.3	4875-5800	1.0-1.2
24/09/2003	PKS 1932-46	B/MIT/G600B/-	3*900	9	1.3	3000-4900	0.7-1.0
		R/MIT/G600RI/GG435+81	3*900	9	1.3	4900-6700	0.7-1.0
25/09/2003	PKS 2135-20	B/MIT/G600B/-	3*900	52	1.3	2250-3600	1.3-1.6
		R/MIT/G600RI/GG435+81	3*1200	52	1.3	3600-5000	1.3-1.6
24/09/2003	NGC 612	B/MIT/G600B/-	3*900	-13	1.3	3500-5855	0.6-0.9

reddening and redshift ( $K$ -correction) effects, unlike broad-band colour comparisons. (e.g. Smith & Heckman 1989).

Figure 1 shows the spatial distribution of the continuum flux in the two regions around 4000Å for all sources in the sample along with the derived  $D(4000)$  ratio. For comparison, expected  $D(4000)$  ratios in the 3750-3850Å bin are overplotted. These ratios were derived using the Bruzual & Charlot (2003) spectral synthesis models (hereafter BC03) for a 12.5 Gyr old stellar population, formed in an instantaneous burst with solar metallicity and a Salpeter initial mass function (IMF). The various comparison  $D(4000)$  ratios comprise: a) a 12.5 Gyr elliptical with solar metallicity, b) a 12.5 Gyr elliptical with sub-solar metallicity ( $Z = 0.4 Z_{\odot}$ ), c) a 12.5 Gyr elliptical diluted with a flat spectrum such that the 12.5 Gyr population accounts for i) 50% and ii) 25% of the continuum flux.

All sources in the sample show a significant UV excess compared to a passively evolving old (12.5 Gyr), solar metallicity elliptical galaxy. For all galaxies in the sample, the  $D(4000)$  ratio suggests that only 25-50% of the flux in the UV originates from the 12.5 Gyr stellar population. Interestingly, for those sources that are spatially resolved (3C 236, 3C 218, 3C 321, 3C 285, 3C 433, PKS 0023-26, NGC 612), *the UV excess is also spatially extended, covering the entire spatial extent of the galaxy*, suggesting that, whatever causes the UV excess (AGN continuum and/or a YSP) is important *galaxy wide*, and is not confined to the nuclear

regions. Further, some objects show interesting trends in their UV excess. In 3C 218, the UV excess increases symmetrically towards the centre of the galaxy. In contrast, the UV excess in NGC 612 decreases symmetrically towards the nucleus. It is also notable that, in the case of the double nucleus systems 3C 321 and 3C 433, the UV excesses extend across both nuclei as well the extended haloes of the systems.

The spatial continuum profiles in Figure 1 have been used to identify regions of interest in the 2-dimensional spectra for extraction and continuum modelling (see below). For the majority of objects, only a central nuclear aperture was extracted. Notable exceptions are NGC 612, 3C 433 and 3C 321. All apertures are marked on Figure 1. Our complete spectra cover a wide wavelength range, vital for accurate modelling of the SEDs, and the observed rest wavelength ranges for each object are summarised in Table 2.

## 4.2 The nebular continuum

Prior to continuum modelling, a nebular continuum was generated for each aperture to be analysed over the entire wavelength range. This comprises the blended higher Balmer series ( $> H8$ ) and a theoretical nebular continuum (generated using the STARLINK package DIPSO, which includes the effects of free-free emission, free-bound recombination and

two-photon continua) following Dickson et al. (1995). Both components of the nebular continuum were normalised to the  $H\beta$  flux in each emission line component. Note,  $H\beta$  was modelled using the minimum number of Gaussian components required to give a physically viable good fit and so for many apertures, in particular the nuclear aperture, the generated nebular continuum included multiple components, as discussed in Holt et al. (2003) for the complex nuclear aperture in PKS 1345+12. The spectra of several of the objects are subject to significant reddening. Hence, the nebular continuum was generated using the *de-reddened*  $H\beta$  line fluxes and then *re-reddened* before being subtracted from the galaxy spectrum. The degree of internal reddening was estimated using the Balmer line decrements (e.g.  $H\alpha/H\beta$ ,  $H\gamma/H\beta$ ) and estimated separately for the different kinematic components of the lines in each aperture.

It should be noted that, when generating the nebular continuum, one must carefully consider the potential pitfalls. In sources where a significant fraction of the optical/UV light originates from a young stellar component, the Balmer lines (particularly  $H\beta$ ,  $H\gamma$ ) may be affected by underlying stellar absorption lines, and the flux therefore under-estimated. To check on the likely impact of the stellar absorption lines, we have followed the technique of Holt (2005) and subtracted off the best fitting continuum model and then re-measured the emission lines.

Considering these issues, the checks show that the spectra fall into three categories: i) apertures in which the original and re-calculated nebular continua based on  $H\alpha/H\beta$  are similar (within a few percent in the 3450-3550Å bin; e.g. PKS 0039-44) – we find that, due to this effect,  $H\beta$  is typically under-estimated by  $\lesssim 10$  per cent. Further, in apertures where reddening is important, a 10 per cent correction on the  $H\beta$  flux, gives a variation in the  $E(B-V)$  value of only  $< 0.1$  for  $H\alpha/H\beta < 10$ . For a discussion regarding the extinction law used, see Section 5.2; ii) apertures in which the nebular continuum fraction is so small ( $\lesssim$  few per cent) that even large differences in nebular reddening would not significantly affect the results (e.g. 3C 218, 3C 236, NGC 612) and iii) apertures in which the reddening estimate was based solely on weaker lines (e.g.  $H\gamma$ ,  $H\beta$ ) due to  $H\alpha$  lying outside of the observed spectral range (e.g. PKS 0023-26, PKS 2135-20, PKS 1932-46). For case iii), we are less confident of the reddening estimate due to uncertainties in measuring  $H\gamma$  as it is a weak, blended line which is relatively more affected by underlying stellar absorption features than  $H\alpha$  or  $H\beta$ . In these apertures, we have followed the example of PKS 1345+12 as discussed in Holt et al. (2003)<sup>2</sup> which allows us to determine the maximum nebular continuum fraction, i.e. that which does not produce an unphysical step-function in the data at the location of the Balmer break when subtracted. For these apertures, we have modelled the continuum twice, with both the maximum and minimum (i.e. 0%) nebular continuum fraction (this technique was also used for PKS 1549-79; see H06). Reassuringly, we find that the modelling results are similar for both cases of nebular continuum sub-

traction (minimum and maximum). Assuming a zero nebular continuum fraction gives a slightly larger UV continuum flux and so would potentially shift the  $\chi^2_{\text{red}}$  minimum to slightly younger ages. For apertures in which the continuum is dominated by a power-law component (e.g. PKS 1932-46) and/or the YSP age is poorly constrained (e.g. PKS 2135-20), the modelling results based on both the minimum and maximum nebular continua are indistinguishable i.e. the effect on our results due to errors on the subtracted nebular continuum are insignificant. In the nuclear aperture of PKS 0023-26, the YSP contribution is large (50-60%) and has a tightly constrained minimum (see Figure 3). For this case, subtracting off the maximum nebular continuum (22.5%) gives a YSP age range of 0.03-0.05 Gyr whilst a zero nebular continuum model gives a YSP age range of 0.01-0.03 Gyr. We are therefore confident that the uncertainties in the nebular continuum subtraction do not significantly affect our results.

The contribution of the nebular continuum (reddened where necessary) to the flux in the 3540-3640Å bin in each aperture ranges from  $\lesssim 1\%$  (NGC 612, 3C 381, mid aperture in 3C 321) to  $\sim 25\%$  (extended aperture of 3C 321, PKS 1932-46) and is summarised in Table 3.

For the objects with published nebular continuum measurements, the nebular continuum fraction previously estimated is typically higher than the estimates here. For the sources in the 2Jy sample (PKS 0023-26, PKS 0039-44, PKS 0409-75, PKS 1932-46 and PKS 2135-20 – see Tadhunter et al. 2002), the differences are likely to be due to the fact that Tadhunter et al. (2002) made no correction for reddening, stating that these nebular continuum fractions were upper limits. In this paper, we have followed the careful reddening correction technique described in Holt et al. (2003) and generally derive lower nebular continuum fractions.

### 4.3 Continuum modelling

After subtracting the nebular continuum, the continuum SEDs were modelled using CONFIT, a purpose written IDL code using a minimum  $\chi^2$  technique (Robinson 2001). The program allows up to three continuum components to be combined – up to two different stellar populations, with or without a power-law component. Note that the power-law could represent an AGN/scattered light component or a very young stellar population. The stellar templates used in the modelling were taken from the 2003 version of the spectral synthesis results of Bruzual & Charlot (2003; hereafter BC03). The stellar population ages used include old, evolved stellar populations (OSP: 12.5 Gyr and, in some cases, 7.0 Gyr) and various young stellar populations (YSP: 0.01-5.0 Gyr in varying steps). All stellar population models assume a Salpeter initial mass function (IMF), solar metallicity, instantaneous starburst. The YSP spectra were reddened over the range  $0.0 < E(B-V) < 1.6$  in steps of 0.1 using the Seaton (1979) extinction law (see Section 5.2). Finally, when a power-law component was included (of the form  $F_\lambda \propto \lambda^\alpha$ ), the spectral index of the power-law was allowed to vary between -15.0 and 15.0 (to ensure reasonable calculation times).

Various models were tried including:

<sup>2</sup> As the technique for correcting for the nebular continuum used here is discussed in detail in Holt et al. (2003), we do not discuss the technique or show examples of the generated nebular continua.

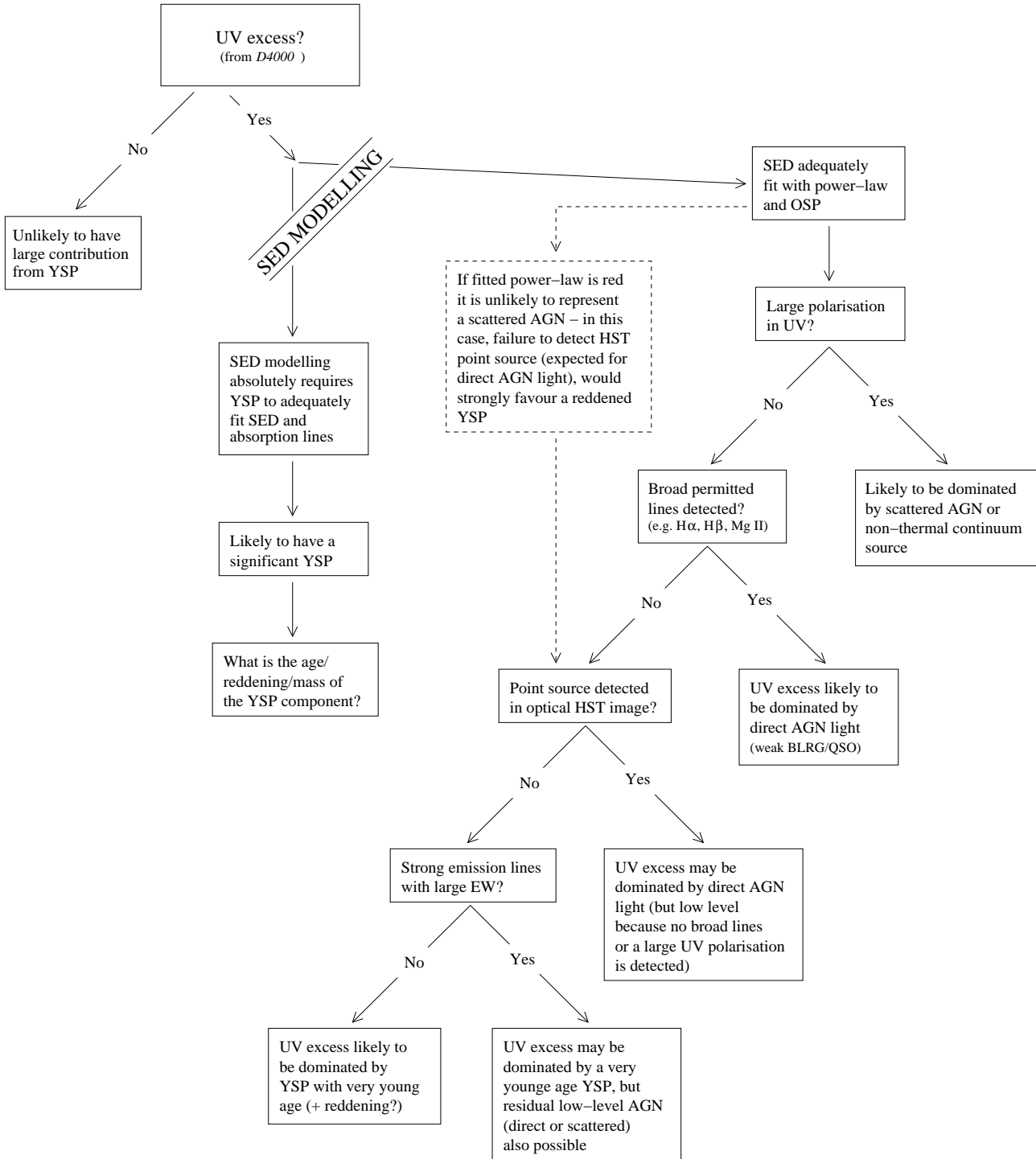


**Figure 2.** The ‘decision tree’ used to interpret the modelling results. Abbreviations are as follows: SED: spectral energy distribution; YSP: young stellar population; OSP: old stellar population; EQW: equivalent width; BLRG: broad line radio galaxy; QSO: quasar;  $D4000$ : ratio of continuum fluxes at the  $4000\text{\AA}$  break.

- an OSP (12.5 Gyr) with zero reddening.
- an OSP (12.5 Gyr, zero reddening) with a power-law component.
- an OSP (12.5 Gyr, zero reddening) with a YSP ( $0.01 < t_{\text{YSP}} < 5.0$  Gyr,  $0.0 < E(B-V) < 1.6$ ).
- an OSP (12.5 Gyr, zero reddening) with a YSP ( $0.01$

$< t_{\text{YSP}} < 5.0$  Gyr,  $0.0 < E(B-V) < 1.6$ ) and a power-law component.

- for the higher redshift sources (e.g. PKS 2135-20, PKS 0039-44, PKS 0409-75 and PKS 0023-26), ‘younger’ old stellar populations were also tried for all four combinations above including 7.0 Gyr, 9.0 Gyr and 10.0 Gyr because, at

the redshifts of these objects, current cosmological models show the universe is younger than 12.5 Gyr.

Our general philosophy is to model the data with the minimum number of stellar and/or power-law components that provide an adequate fit to the spectra. Given that the galaxies we are modelling are all early-type in terms of their optical morphologies, we start by assuming that all galaxies contain an old (7 – 12.5 Gyr) stellar population (OSP) at some level, and that any young stellar populations were formed in a single instantaneous burst as a result of a merger, and hence have a particular age. In our models very young, reddened YSPs (<10 Myr) may be simulated by adding a power-law component, provided that they can be distinguished from AGN-related components (see below). Clearly more components would be required to model more complex star formation histories, but the greater the numbers of components, the greater the likelihood of degeneracies in the solutions.

One of the major ambiguities in our model solutions is that we cannot readily distinguish between the case of a highly reddened very young YSP (<10 Myr) plus an OSP, and an AGN-related power-law plus an OSP, based on the SED modelling alone. This is because the spectra of the very young YSPs are relatively featureless in terms of the strengths of the absorption lines and the amplitude of the Balmer break (e.g. González Delgado et al. 1999, 2005). Therefore it is necessary to use auxiliary information, such as UV polarisation, detection of point sources in HST images, detection of broad permitted lines, and emission line luminosity to distinguish between these cases. For example, if the UV excess is predominantly caused by a scattered AGN component, revealed as a power-law in the SED fits, we expect to measure significant UV polarisation and a relatively flat or blue power-law slope ( $\alpha < 0.5$ )<sup>3</sup>. On the other hand we expect a direct AGN component (from a low-luminosity or partially obscured quasar) to be associated with the detection of broad permitted lines and a point source in HST images. Figure 2 presents a flow diagram of the decision making process involved in interpreting the modelling results for such cases.

For the modelling, continuum bins were selected to avoid emission lines and, in the case of 3C 285, 3C 433, 3C 218/Hydra A, 3C 321 and 3C 381, the uncorrected atmospheric absorption bands. Typically, 40-50 bins were chosen for each aperture to ensure good sampling over a large spectral range as evenly distributed in wavelength as possible. In addition, a normalising bin in the blue part of the spectrum, common to all objects, was chosen with rest wavelength 4720-4820 Å. The CONFIT program then generated the models by scaling the different components to the flux in the normalising bin so the total model flux was <125 per cent of the observed flux<sup>4</sup>, finding the model combination with the minimum reduced  $\chi^2$  ( $\chi_{\text{red}}^2$ ). For the  $\chi_{\text{red}}^2$  determi-

nation, we assume a relative flux calibration error of  $\pm 5$  per cent.

Combining the best fitting model for each combination of OSP with reddened or unreddened YSPs of various ages (both with and without a power-law component) forms a surface in  $\chi_{\text{red}}^2$  for YSP age versus E(B-V) from which contour plots can be generated. Examples of the contour plots of the  $\chi_{\text{red}}^2$  space for each aperture requiring a YSP component are shown in Figure 3. Using these plots, we identified minima<sup>5</sup> in the  $\chi_{\text{red}}^2$  space to be further investigated using detailed comparisons of the stellar absorption features known to be sensitive to age. The CaII K $\lambda$ 3968, the G-band (4306Å) and the Mg Ib band (5173Å) absorption features are particularly important for such comparison because they are not significantly infilled by emission lines. In some cases with weak emission lines it was also possible to use the higher order Balmer line features for detailed comparisons. Along with examples of the overall SED fits, detailed comparisons of the region containing the Balmer series and CaII H+K are shown in Figure 4.

Note that, when discounting models on the basis of detailed fits to CaII K feature, consideration must be made of the potential contribution of intrinsic ISM absorption to the to this feature, especially in highly reddened cases. A contribution from the ISM would strengthen the CaII K line in the observed spectrum, but not in the model spectra. Therefore models that underpredict the observed strength of CaII K may be viable, whilst models which significantly overpredict the strength of CaII K can be discounted. This technique proved particularly useful in distinguishing between two clear minima in the  $\chi_{\text{red}}^2$  space (e.g. 3C 285). In some cases it was necessary to apply smoothing to the models to obtain good matching in the absorption lines because the models and the data have different effective resolutions.

Hence, in order to be considered a viable fit to the data, the various models had to provide *both a good fit to the overall SED and the stellar absorption lines*. When relying on one technique alone, the solutions are often degenerate in age/reddening space for the YSP (see also Tadhunter et al. 2005).

#### 4.3.1 Hydra A (3C 218)

3C 218 is one of the most powerful radio galaxies in the local universe, however, despite having a radio luminosity more than an order of magnitude larger than the characteristic break luminosity between the FR I and FR II classes, its morphology is edge darkened — more characteristic of FR I sources (e.g. Baum et al. 1988).

3C 218 is optically identified with Hydra A (Simkin 1979), the dominant cD2 galaxy in the centre of a poor but X-ray luminous (e.g. David et al. 1990) cluster. Hydra A has a double nucleus with the second nucleus lying  $\sim 7$  arcsec SE of the active nucleus, within the common envelope (Hansen et al. 1996). Like a significant number of

<sup>3</sup> Such blue power-law slopes have been measured for all cases with significant scattered AGN components (Tadhunter et al. 1996; Tran et al. 1998; Cohen et al. 1999; Vernet et al. 2001) and strong emission lines – the objects with the strongest scattered AGN components tend to be those with the most luminous emission lines (see Tadhunter et al. 2002)

<sup>4</sup> The maximum allowed model flux is greater than 100 per cent

of the measured flux to allow for uncertainties in the measured flux and models in the bin.

<sup>5</sup> Note, whilst the main discriminating factor is the *minimum* in the  $\chi_{\text{red}}^2$  space, all fits with  $\chi_{\text{red}}^2 \lesssim 1$  are deemed to be a ‘good fit’. In addition, fits with  $\chi_{\text{red}}^2 \lesssim 1.2$  are also considered for the detailed comparisons. See detailed discussion in Tadhunter et al. (2005).



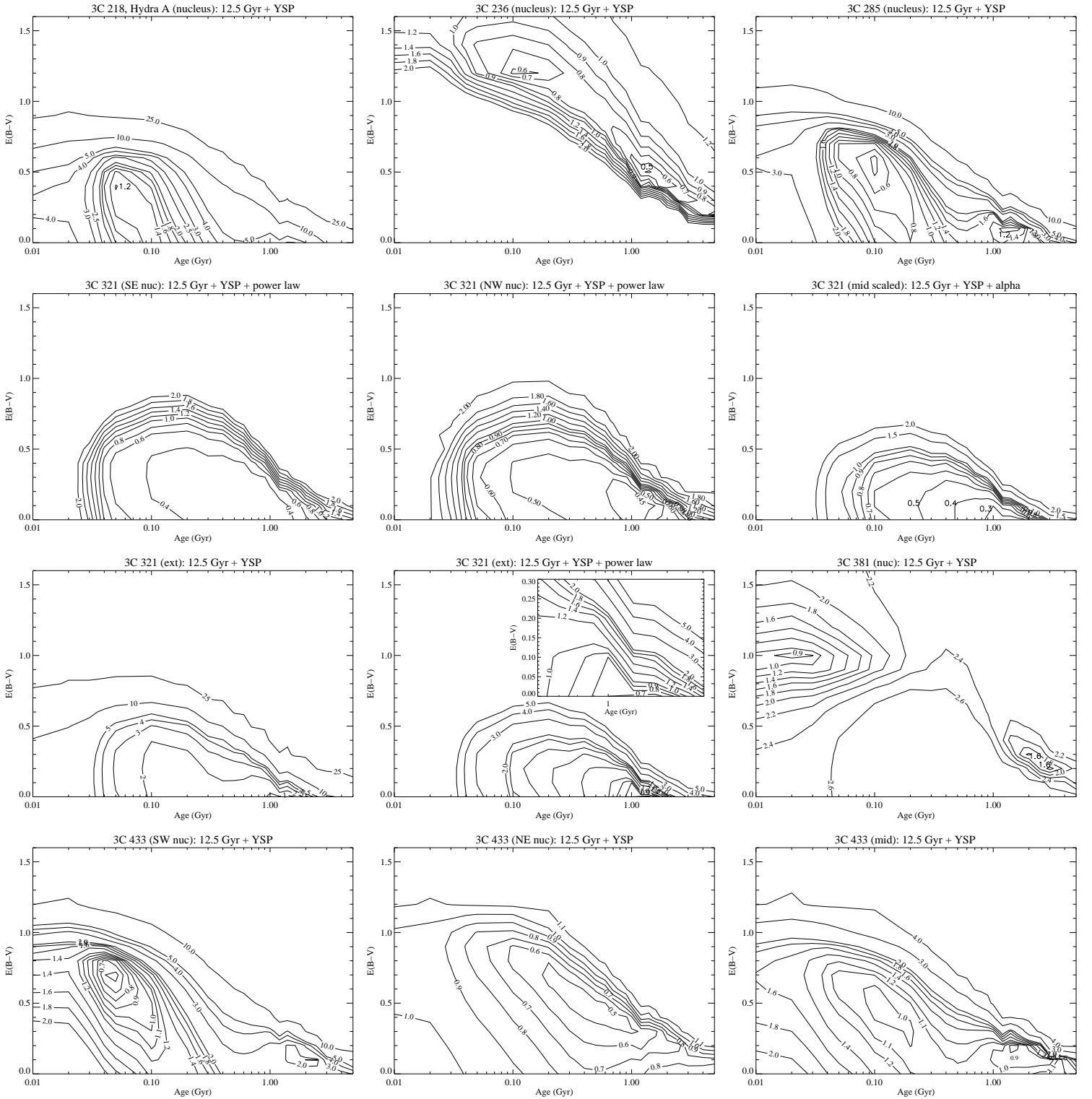


**Figure 3.** Contour plots of the reduced chi squared space ( $\chi^2_{\text{red}}$ ) for all combinations of age (x axis) and reddening (y axis) of the YSP for all apertures requiring a YSP component. All plots assume the Seaton 1979 reddening law *except* for the second (labelled) plot for the nuclear aperture of NGC 612 which uses the Calzetti et al. 2000 reddening law. For descriptions of the plots see Section 4.3. In general, we show one contour plot for each aperture. For apertures where a power-law component is expected, the plot is for models with an OSP, a YSP and a power-law component. For apertures in which a power-law component is not expected (e.g. due to location, the weakness of emission lines), the contour plot is for models with an OSP and a YSP only. Where the contours in the region of the minimum are crowded, a zoom of this region is shown inside the plot. Note, a contour plot is not shown for PKS 0039-44. Two plots for the nuclear aperture of NGC 612 are presented, the first using the (Seaton 1979) extinction law and the second using the (Calzetti et al. 2000) law. These plots illustrate how the different reddening laws may influence the result. The plots clearly show that, whilst the details of the models may vary, the differences between the reddening laws do not change the overall result within a certain tolerance. We discuss the different reddening laws further in Section 5.2 and Figure 10

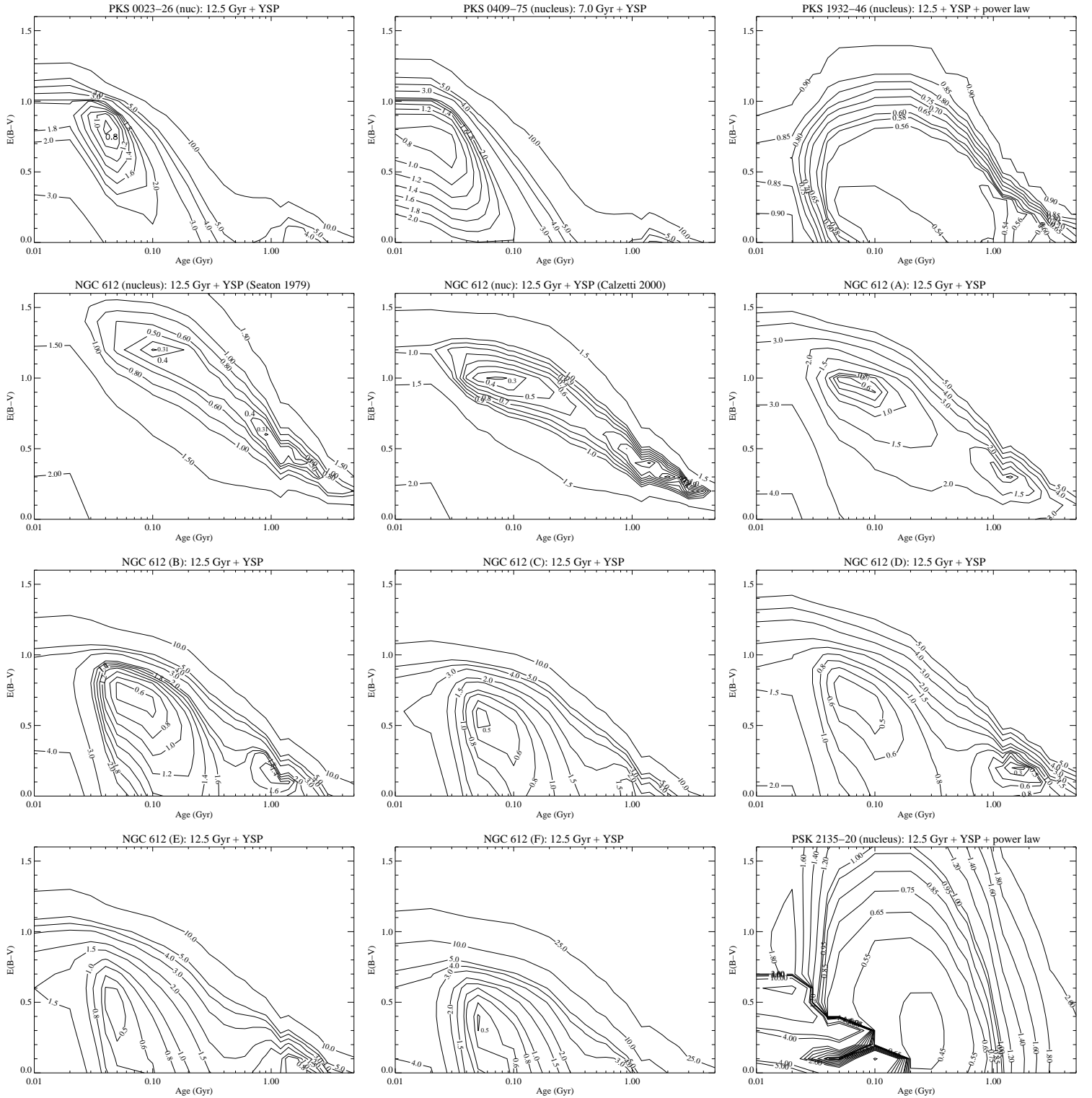


**Figure 3.** Contour plots *continued*.

radio galaxy hosts, the optical colours of 3C 218 are blue in comparison to normal elliptical galaxies (see also Figure 1). Several authors have attributed these colours to a massive ( $10^8$ - $10^9 M_{\odot}$ ) burst of star formation occurring  $\sim 50$  Myr ago (e.g. McNamara 1995; Hansen et al. 1996). Optical spectroscopy supports this view with the detec-

tion of a prominent Balmer series in the nuclear spectrum (Hansen et al. 1996; Melnick et al. 1997; Aretxaga et al. 2001; Wills et al. 2004). Using a variety of line and break indices, Aretxaga et al. (2001) attribute the blue-subtracted continuum to a 0.007-0.04 Gyr old starburst dominated by B-type giant/supergiant stars. Spectral syn-

thesis modelling by Wills et al. (2004) finds results consistent with Aretxaga et al. (2001) although their best-fit model suggests the starburst occurred at the earlier end of this range, 0.05 Gyr ago.

In this paper we have repeated the optical spectral modelling of Wills et al. (2004) using new, deeper spectra with wider spectral coverage, and using the latest generation of high resolution spectral models of Bruzual & Charlot (2003).

As discussed above, and shown in Figure 1, 3C 218 has a clear UV excess and the prominent Balmer series makes it a strong starburst candidate. Indeed, as reported by Wills et al. (2004), we find that the SED cannot be adequately modelled without a YSP component. Hence, we have modelled the SED with an OSP and a YSP both with and without a power-law component. In Figures 3 and 4 we only show the case of an OSP plus a YSP – in common with many other cases, adding a power-law gives a similar shape to the  $\chi_{\text{red}}^2$  space with a similar position for the  $\chi_{\text{red}}^2$  minimum although the number of solutions giving a viable fit to the overall shape of the SED is dramatically increased. Whilst including a power-law component gives many viable fits, there is no strong observational evidence for a power-law component in 3C 218. Despite harbouring a powerful radio source, the optical emission lines are relatively weak (we have not corrected for the nebular continuum) and there is no strong point source in any of the published images (e.g. McNamara 1995 – ground based).

For fits without a power-law component, one clear minimum is observed at 0.05 Gyr with significant reddening ( $E(B-V) = 0.4$ ;  $\chi_{\text{red}}^2 = 1.2$ ) accounting for 50% of the continuum flux. In fact, only YSPs with ages 0.05-0.1 Gyr with similar reddening provide acceptable fits to the SED modelling and, even when the detailed fits are used, it is difficult to distinguish between them. By combining the fits to the lines and the continuum around them, overall the best fit is for the OSP plus a 0.05 Gyr YSP. This result is entirely consistent with the findings of Wills et al. (2004), although our results require a significantly larger contribution of the YSP (c.f. 10-30% in Wills et al. 2004), and towards the older end of the range reported by Aretxaga et al. (2001).

Including a power-law component dramatically increases the number of models providing a good fit, marginally improves the  $\chi_{\text{red}}^2$  and shifts the minimum to slightly older ages; OSP + YSP (0.1 Gyr,  $E(B-V) = 0.2$ , 47% contribution). Hence, for the nuclear region of Hydra A we find the best fitting model to be an old (12.5 Gyr) stellar population (45%) with a YSP (0.05 Gyr,  $E(B-V) = 0.4$ , 50% contribution). This is entirely consistent with the findings of both Wills et al. (2004) (the difference in flux percentage is likely to be due to differences in the seeing and extraction aperture) and towards the older end of the range reported by Aretxaga et al. (2001). Wills et al. (2004) also attempted to model the spectrum with *younger* age ‘old’ stellar populations. They found the best fit comprised a 2 Gyr population (89%) with a 0.05 Gyr YSP (11%). We have also attempted to model the nuclear spectrum of Hydra A with ‘younger’ old populations and found this made no difference to our overall result.

#### 4.3.2 3C 236

The radio source 3C 236 and its host galaxy are peculiar at both optical and radio wavelengths. The radio source exists both on the large scale (a classical double source extends to  $\sim 4$  Mpc, making it the largest known radio source, e.g. Schilizzi et al. 2001) and yet the nuclear regions harbour a second, compact (2 kpc) radio source suggesting it belongs to the class of ‘double-double’ radio sources (e.g. Kaiser et al. 2000). On the basis of radio spectral ageing techniques and the detection of different star forming regions, two of which are relatively young (of order  $10^7$  yr) and two which are significantly older (of order  $10^8$ - $10^9$  yr, comparable to the age of the giant radio source), O’Dea et al. (2001) argue that this strange radio morphology is the result of a period of fuel starvation of the AGN which lasted around  $10^7$  years before new fuel was provided and the radio source restarted. Note, the relative locations of the radio jets and the star forming regions preclude jet-induced star formation, but the timescales are consistent with a common origin of fuel such as the infall of gas to the host galaxy (O’Dea et al. 2001).

At optical wavelengths the deep ground-based images of Smith & Heckman (1989) reveal the presence of shells and twisted isophotes that are suggestive of a past merger or interaction with a companion galaxy. On smaller scales, HST imaging shows the isophotes of the host galaxy to be flattened and inclined, with a broad asymmetric dust lane on scales of a few kpc which is itself misaligned with the inner disk (e.g. Martel et al. 1999; de Koff et al. 2000). They also show a second,  $\sim 1$  kpc scale dust feature (de Koff et al. 2000). In the UV, three clear knots of emission are detected which trace an arc coinciding with the SE edge of the larger dust lane (Allen et al. 2002; O’Dea et al. 2001).

The integrated nuclear spectrum of 3C 236 has a clear UV excess (Figure 1). We find that the overall SED and the stellar absorption features can be satisfactorily reproduced ( $\chi_{\text{red}}^2 = 1.1$ ) with an old (12.5 Gyr) stellar population (87%) and a red power-law component ( $\alpha = 3.6$ , 12% contribution) and this model is shown in Figure 4.

The power-law component required in this model is red. Following our ‘decision tree’ (Figure 2), a red power-law component is unlikely to be a scattered AGN component and is more likely to be either direct AGN light or a young reddened YSP component. The HST images of Martel et al. (1999); de Koff et al. (2000) and O’Dea et al. (2001) do not show a point source in the nucleus. Hence a large direct AGN light contribution is unlikely. Further, after subtracting the best-fit model we see no evidence for broad emission line components also expected if we are viewing the AGN directly. Hence, the UV excess is likely to be dominated by a very young YSP component which is heavily reddened.

Figure 3 shows the  $\chi_{\text{red}}^2$  space for an OSP plus a YSP component. Two clear minima are observed for YSPs with ages 0.1 Gyr ( $E(B-V) = 1.2$ ,  $\chi_{\text{red}}^2 = 0.58$ ) and 1.4 Gyr ( $E(B-V) = 0.5$ ,  $\chi_{\text{red}}^2 = 0.48$ ), although viable models ( $\chi_{\text{red}}^2 < 1.0$ ) to the SED are found across all ages. Detailed comparisons with the stellar absorption features rule out models with ages  $\gtrsim 1.0$  Gyr because such models overpredict the depth of CaII K feature, although it is difficult to discriminate further. An example of a two component model is shown in Figure 4: 12.5 Gyr (84%) plus 0.05 Gyr YSP (15%,

$E(B-V) = 1.4$ ) with  $\chi_{\text{red}}^2 = 0.78$ . Including a power-law component expands the number of viable fits. In summary, for the OSP plus YSP models, both with and without a power-law component, the YSP contributes typically 10-30% of the flux in the normalising bin for YSP ages  $< 1.0$  Gyr. Hence, our spectral fitting results are consistent with both age estimates derived from HST photometry of O’Dea et al. (2001) –  $\sim 10^7$  yr and  $\sim 10^{8-9}$  yr – for different bright knots in the halo.

#### 4.3.3 3C 285

The double-lobed FR II radio galaxy 3C 285 is identified with an elliptical galaxy, the brightest in a group of galaxies (Sandage 1972). A chaotic morphology consisting of a distorted S-shaped envelope aligned with another galaxy  $\sim 40$  arcsec to the NW (Heckman et al. 1986; Roche & Eales 2000), tidal tails and fans, irregular dust lanes and knots of emission (Allen et al. 2002) and a  $B - V$  colour significantly bluer than a normal elliptical galaxy (Sandage 1972) all provide evidence that the galaxy has undergone a recent merger or interaction with a companion. The UV/optical continuum of 3C 285 has been previously modelled by Aretxaga et al. (2001). By fitting the 4000Å break, they conclude the blue light in the inner 2 arcsec is dominated by a starburst component with an age of 10-12 Myr. In addition, van Breugel & Dey (1993) have investigated the knot of UV emission located halfway between the nucleus and the eastern radio lobe and found the  $UBV$  colours and the 4000Å break to be consistent with a 70 Myr starburst, that may have been triggered by the passing radio jet.

The nuclear spectrum of 3C 285 is highly indicative of a major contribution to the continuum flux by light from young stars – the Balmer sequence is clearly observed in absorption and the galaxy displays a clear UV excess (Figure 1). Indeed, SED modelling excluding a YSP contribution failed to provide an adequate fit to the overall shape of the continuum spectrum.

Whilst it is necessary to have a YSP component to model the SED, good fits are obtained both with and without an additional power-law component. However, the emission lines are relatively weak and HST imaging does not reveal a strong point source; rather, the nucleus is obscured by one of the dust lanes (Allen et al. 2002; Madrid et al. 2006). Models including a power-law can therefore be excluded for two reasons: i) models requiring a very young YSP do not require a power-law component and ii) models with an older age YSP require a large power-law contribution. We have therefore focussed on models which exclude a power-law component. The contour plot for the  $\chi_{\text{red}}^2$  space for a 12.5 Gyr OSP and a YSP is shown in Figure 3.

3C 285 is an ideal example to highlight the degeneracy in the solutions when relying on SED modelling alone – Figure 3 shows two clear minima, one with a young (0.04-0.2 Gyr), reddened ( $E(B-V) < 0.5$ ) YSP contributing 30-50% of the flux in the normalising bin and another for a significantly older (1.0-3.0 Gyr), unreddened YSP ( $E(B-V) < 0.2$ ) contributing  $\sim 100\%$  of the flux in the normalising bin. Detailed comparisons reveal that, whilst the fits to the majority of the diagnostic lines are indistinguishable, the viable models with an older YSP ( $\gtrsim 1.0$  Gyr) significantly overpredict the strength of the CaII K line. Further, models with YSPs  $<$

0.1 Gyr do not fit either the absorption lines or the continuum in the 3700-4300Å region or the G band as well as other models.

Hence, by combining both techniques, it is likely that the nuclear region of 3C 285 contains a significant YSP with age 0.1–0.5 Gyr and reddening  $0.2 < E(B-V) < 0.0$ , contributing 33%–39% of the continuum flux in the normalising bin. An example of a good fit is shown in Figure 4: 12.5 Gyr (72%) + 0.2 Gyr with  $E(B-V) = 0.2$  (33%);  $\chi_{\text{red}}^2 = 0.74$ . The age we estimate is at least an order of magnitude larger than that found by Aretxaga et al. (2001) using the Balmer and 4000Å breaks and line indices (10-12 Myr). Aretxaga et al. (2001) give no indication of the scale of the YSP contribution to the flux.

#### 4.3.4 3C 321

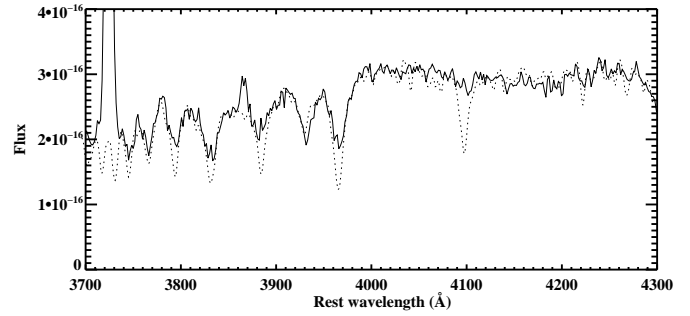
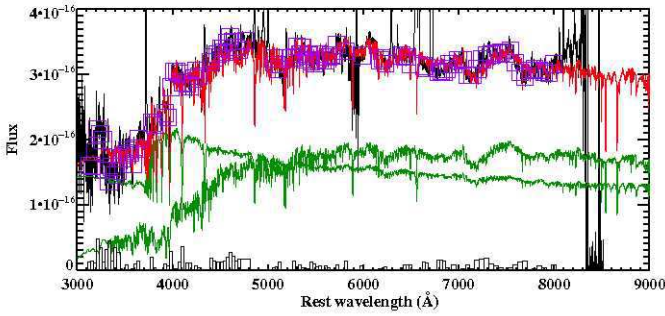
The powerful FR II radio source 3C 321 is identified with a peculiar galaxy with two nuclei separated by  $\sim 3$  arcsec (Spinrad et al. 1985; Heckman et al. 1986; Baum et al. 1988) surrounded by an extended halo of line emission (McCarthy et al. 1995), as well as continuum arcs and tails suggestive of a recent merger (Heckman et al. 1986; Smith & Heckman 1989; Roche & Eales 2000). Similar to a significant number of powerful radio sources, 3C 321 is blue in colour compared to normal elliptical galaxies (Smith & Heckman 1989). Figure 1 also highlights the spatially resolved UV excess.

The SE nucleus is brighter and more closely coincident with the radio core whilst the NW nucleus is clumpy (Zirbel & Baum 1998) but also associated with a peak in the radio emission which then extends as a long (35 arcsec) jet beyond this nucleus (Roche & Eales 2000). However, it is interesting to note that the narrow emission line spectra of the two nuclei have similar line strengths and surface brightnesses (Filippenko 1987; McCarthy et al. 1995).

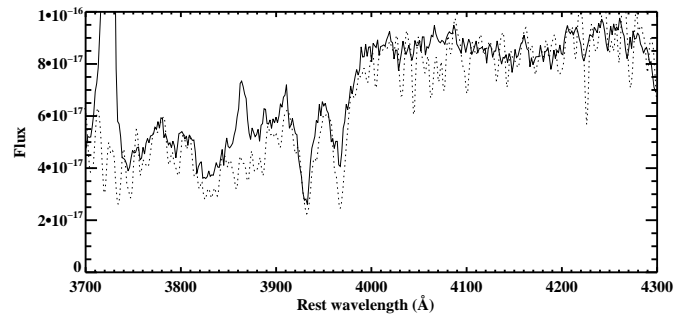
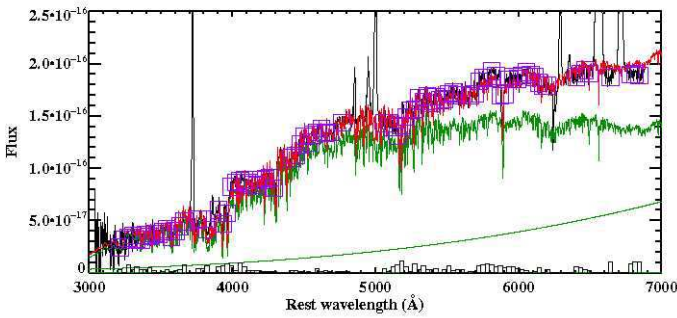
3C 321 is a case in which the scattered quasar component makes a major contribution to the optical continuum, at least in the SE nucleus (Draper et al. 1993). Spectropolarimetry observations of the SE nucleus reveal a high degree of polarisation in the near UV (Tadhunter et al. 1996), as well as broad quasar-like permitted lines in the polarised intensity spectrum (Cohen et al. 1999). However Tadhunter et al. (1996) and Robinson et al. (2000) have demonstrated that it is not possible to model the continuum SED solely in terms of an OSP plus a power-law or quasar template, but that a significant contribution from a YSP is required to fit the spectrum, particularly in the region of the Balmer break. Although they detected a YSP component, Tadhunter et al. (1996) and Robinson et al. (2000) considered only unreddened YSP models, and were unable to pin down the age of the YSP.

3C 321 is spatially well-resolved although, in contrast to Robinson et al. (2000), we have extracted only four apertures. These are shown in Figure 1, which also highlights the significant UV excess observed across the *entire* galaxy. Despite the fact that Robinson et al. (2000) have already presented work on these spectra, we have re-calibrated the data to improve the flux calibration and our analysis uses the latest high resolution models from Bruzual & Charlot (2003) as well as consideration of the reddening of the YSP component.

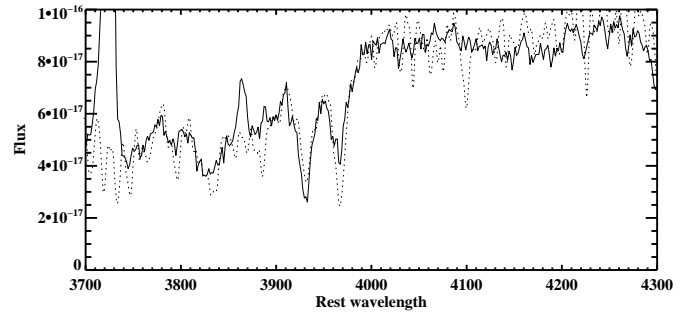
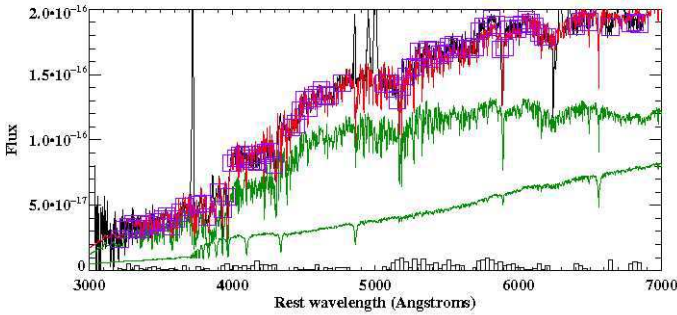
3C 218 (Hydra A): 12.5 Gyr OSP + 0.05 Gyr YSP ( $E(B-V) = 0.4$ )



3C 236: 12.5 Gyr OSP + power law



3C 236: 12.5 Gyr OSP + 0.05 Gyr YSP ( $E(B-V) = 1.4$ )



3C 285: 12.5 Gyr OSP + 0.2 Gyr YSP ( $E(B-V) = 0.2$ )

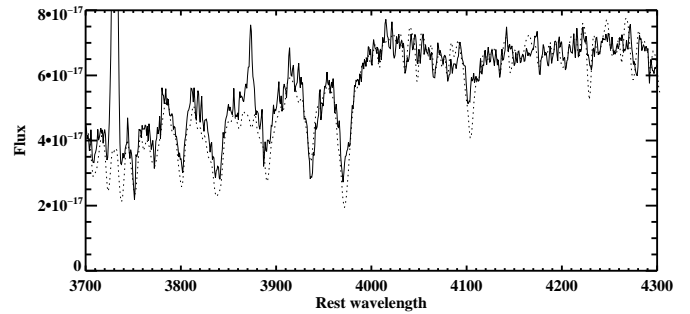
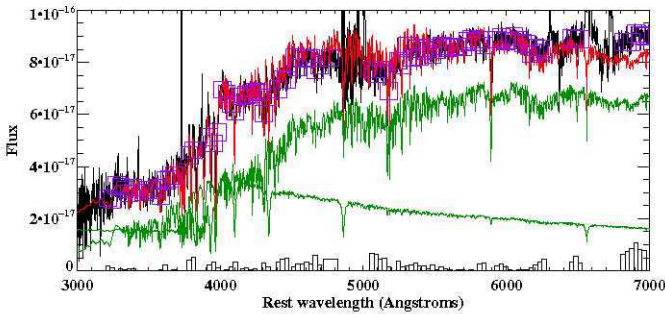


**Figure 4.** SEDs and detailed fits. Left: overall fit to SED where the black line traces the data, the red line is the overall model with one or more components (OSP, YSP, power-law) represented by the green lines. The wavelength bins used to evaluate the fit are identified by the purple boxes (not to scale) and the histogram gives the residuals in each bin. Right: detailed fits in the regions of the Balmer and Ca II lines. The solid line traces the data and the dotted line represents the model (red line in the left hand plots).

**The SE nucleus.** The spectrum of the SE nucleus of 3C 321 shows evidence for the Balmer sequence in absorption and so a YSP contribution is likely to be important. Indeed, previous studies of the continuum emission of 3C 321 (see above) have shown that at least three distinct components are required to model the SED: an OSP, a YSP and a power-law component (the latter representing the scattered quasar indicated by the polarimetry measurements). Note that we cannot obtain viable fits with an OSP and power-law alone ( $\chi_{\text{red}}^2 > 2$ ) in this aperture, consistent with the results of Tadhunter et al. (1996). Hence, we have focussed on the three component fits to the SED.

When including a power-law component, as for many of the sources studied, acceptable fits to the SED were found for most ages of YSP – see Figure 3. Hence, the detailed comparisons proved vital for distinguishing between the models. Using the CaII K line (Figure 4), we can confidently rule out models including a YSP component older than  $\sim 1.0$  Gyr – all models with a YSP age  $\gtrsim 1.0$  Gyr significantly overestimate the depth of the Ca K line – this can not be overcome by smoothing of the models to match the resolution of the data. The youngest ages (0.04, 0.05 Gyr) are also considered unlikely as they do not require a contribution from the power-law component (i.e. 0% contribution in the fits) – previous polarimetric observations combined with the detection of a broad component to H $\alpha$  suggest a contribution of at least 10-20% at the position of our normalising bin (see above). Hence, the SE nucleus in 3C 321 can be well modelled by an OSP (15-55%) plus YSP (age: 0.1-1.0 Gyr, E(B-V): 0.1-0.3, 30-60%) and power law (10-20%) components with  $\sim 0 < \alpha < \sim 0.6$ . Figure 4 shows an example of a model in the best fitting range comprising a 12.5 Gyr OSP (46%), a 0.4 Gyr YSP (E(B-V) = 0.2, 30%) and a power-law component ( $\alpha = 0.1$ , 22%). These results are consistent with those of Tadhunter et al. (1996) and Robinson et al. (2000) in terms of the contribution of the power-law component and the YSP contribution. Note, Robinson et al. (2000) do not find evidence for a YSP in the SE nucleus, only in the more extended regions. However, our SE nuclear aperture is larger than that used by Robinson et al. (2000) and therefore includes light from more extended regions which do have a YSP component.

**The NW nucleus.** As discussed above, whilst the SE nucleus is that identified with the radio source, the second nucleus  $\sim 3$  arcsec to the NW also shows signs of activity – it is close to an enhancement in the radio emission along the jet and has an emission line spectrum similar in strength and ionisation state to the SE nucleus. Further, as demonstrated by Figure 1, its observed UV excess is similar to that observed in the SE nucleus.

As for the SE nucleus, it was not possible to obtain a good fit with an OSP, with or without a power-law ( $\chi_{\text{red}}^2 \sim 2.0$ ), and so a YSP component is likely to be important.

It is possible to model the SED of the NW nucleus with an OSP plus a YSP without a power-law. Viable fits ( $\chi_{\text{red}}^2 \lesssim 1.2$ ) are found for all ages of YSP with the familiar 2 minima degeneracy. The ‘younger’ minimum is for ages  $\sim 0.1$  Gyr (E(B-V) < 0.3) whilst the second minimum is for much larger ages (> 1.0 Gyr). Around the ‘younger’ minimum, the best fits to the lines *and* the continuum are for ages 0.04-0.2 Gyr (12.5 Gyr: 70-75%, YSP: 25-30%) – ages > 0.3 Gyr do not fit the continuum in the region 4000-4300Å well.

Solutions for all ages of YSP can provide good fits to the G-band and Mg Ib features.

Unlike in other apertures we have not been able to distinguish between the two minima. At first glance, the models including the older YSPs (1.0-1.4 Gyr) appear to significantly overpredict the strength of CaII K. However, smoothing of the models to better match the resolution of the data show that for this aperture, the models including older age YSPs can not be confidently ruled out

The strong emission lines detected in the NW nucleus suggest that it also harbours a powerful AGN. Moreover, the results of Draper et al. (1993) show that it is significantly polarised. We have therefore attempted to model the SED of the NW nucleus with a three component model. In common with the two component OSP plus YSP model, we find viable fits for most ages of the YSP (0.05-2 Gyr) with a minimum consistent with the older ages in the two component models at  $\sim 1$  Gyr. The contour plot of the  $\chi_{\text{red}}^2$  space is shown in Figure 3. Detailed fits show that the models including the oldest age YSPs (> 1.6 Gyr) can be ruled out due to the large over-estimate of the Ca K line and the models including the youngest age YSPs (< 0.1 Gyr) are ruled out as they do not include a zero power law component. The remaining models, however, are indistinguishable. Hence, the viable fits have YSP ages 0.1-1.4 Gyr with  $0.1 < E(B-V) < 0.3$  contributing 25-75% of the SED flux. An example of a good fitting model is shown in Figure 4: 12.5 Gyr OSP (52%) plus 0.6 Gyr YSP (E(B-V) = 0.2; 30%) plus a power law (15%;  $\alpha = -0.1$ ) with  $\chi_{\text{red}}^2 = 0.45$ .

**Extended apertures** Because the UV excess is spatially resolved, we have followed the work of Robinson et al. (2000) and extracted a further two apertures, one between the two nuclei and one to the south east of the SE nucleus, marked on Figure 1. Indeed, Robinson et al. (2000) showed that, in the case of 3C 321, the YSP component makes a relatively larger contribution off-nucleus than in the regions of the two nuclei.

**Between the nuclei.** It is not possible to model the region between the nuclei with an OSP or OSP plus power-law component ( $\chi_{\text{red}}^2 > 2$ ). This is not surprising as the spectrum shows clear evidence for a Balmer break and Balmer absorption features, suggesting a strong YSP component. For OSP plus YSP models, viable fits ( $\chi_{\text{red}}^2 \lesssim 1.2$ ) can be obtained for ages 0.05-2.0 Gyr with E(B-V)  $\lesssim 0.4$ , dependent on age – younger YSPs require more reddening. There is also a clear degeneracy with two minima at ages  $\sim 0.1$ -0.2 Gyr and  $\sim 1.0$ -2.0 Gyr. However, examination of the overall fit to the SED shows that whilst the value of  $\chi_{\text{red}}^2$  is low, two regions are not modelled well –  $\sim 5000$ -5500Å and  $\gtrsim 7000$ Å.

As the two component models fail to successfully fit these two regions, we have attempted to model the SED including a power law. Whilst for most off-nuclear apertures we have assumed that a power law component is unlikely, for 3C 321, based on the previous observational results, this is not necessarily the case.

Figure 3 shows the  $\chi_{\text{red}}^2$  space for the three component models. When including a power law, the  $\chi_{\text{red}}^2$  reduces significantly and a broad minimum is found for ages 0.04-2.0 Gyr with reddening E(B-V)  $\lesssim 0.5$ . Combining the large scale and detailed fits, the youngest ages can be ruled out on the basis of the large scale (5000-5500Å and  $\gtrsim 7000$ Å regions) fits (0.04-0.1 Gyr) and the fits to the CaII K line ( $\lesssim 0.3$

Gyr). Older age YSPs ( $> 1.0$  Gyr) can be ruled out as the CaII K line is significantly over-predicted.

Hence, the best fitting models for the region between the nuclei comprise a 12.5 Gyr OSP (30-50%) plus a 0.4-1.0 Gyr YSP ( $E(B-V) = 0.0-0.1$ , 40-60%) and a power law component (5-8% with  $\alpha \sim -1.6 - -1.7$ ). An example of a model in this range is shown in Figure 4: 12.5 Gyr plus 0.4 Gyr YSP ( $E(B-V) = 0.1$ , 39%) plus a power law (8%,  $\alpha = -1.6$ ) with  $\chi_{\text{red}}^2 = 0.42$ .

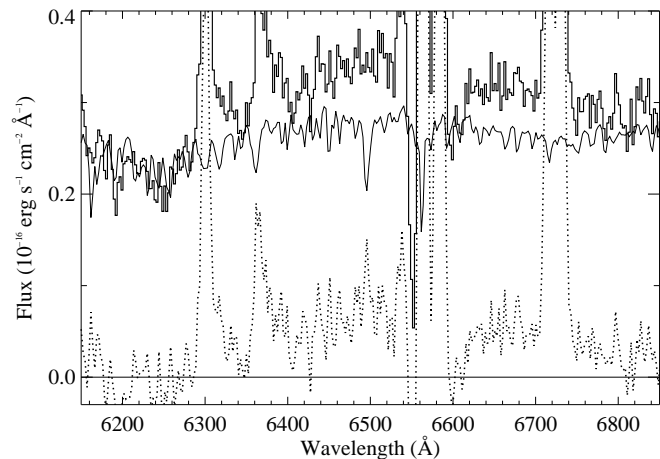
**Extended aperture.** As for the aperture between the nuclei, it is not possible to model the SED with an OSP or OSP plus power-law alone ( $\chi_{\text{red}}^2 > 6$ ). Modelling the SED using two and three components, each incorporating a YSP, shows that, whether or not a power-law component is included, the best fits to the overall SED consistently required a  $\sim 0.7 - 2.0$  Gyr YSP with zero reddening. Figure 3 shows the  $\chi_{\text{red}}^2$  space for both two and three component models. This is reassuring and shows our results are robust against the fine details of the modelling. Detailed comparisons of the absorption lines show that, when a power-law component is excluded, the CaII K line is *always* significantly over-predicted. Including a power-law component has the effect of diluting the absorption features. Indeed, this produces a significantly better fit to the CaII K line for a YSP age of 0.7-1.0 Gyr, whilst older and younger ages give worse fits to either the CaII K line and/or the continuum surrounding the absorption features.

The modelling suggests that three components are required to model the spectrum. A significant YSP component (54-72% of the flux in the normalising bin) is essential to provide a good fit to the SED and detailed comparisons reveal that a small (5-6% of the flux in the normalising bin) power-law component improves the fit to the absorption features. An example of a good fitting model, 12.5 Gyr (21%) plus 1.0 Gyr YSP ( $E(B-V) = 0.0$ ; 72%) plus power-law (5%;  $\alpha = -1.2$ ) with  $\chi_{\text{red}}^2 = 0.7$  is shown in Figure 4. This aperture contains the largest contribution from a YSP ( $> 50\%$  in the normalising bin).

**Summary for 3C 321.** The good spatial resolution of the continuum structure in 3C 321 allows us to investigate the spatially extended UV excess in four distinct regions including both nuclei, the region between the nuclei and an extended aperture to the SE of the active nucleus. Despite the large spatial scale and the different environments analysed, the results are generally consistent. All apertures require a significant contribution ( $\sim 30-70\%$ ) from a  $\sim 0.5-1.0$  Gyr YSP with little reddening ( $E(B-V) \lesssim 0.3$ ) although we can not rule out significantly younger ages in the two nuclei. In addition, all apertures require a relatively small contribution (few-20%) from a power law in all apertures, the largest contribution in the active nucleus.

#### 4.3.5 3C 381

The ultra-steep spectrum radio source 3C 381 is a classical double radio source extending more than 70 arcsec along PA 90 (Riley & Pooley 1975). Optically it is identified with a round high surface brightness galaxy with a compact nucleus. A lower surface brightness companion lies 5.5 arcsec away along PA 65 and the detection of tidal distortions and tails extending N and S confirms 3C 381 is currently interacting with this compan-

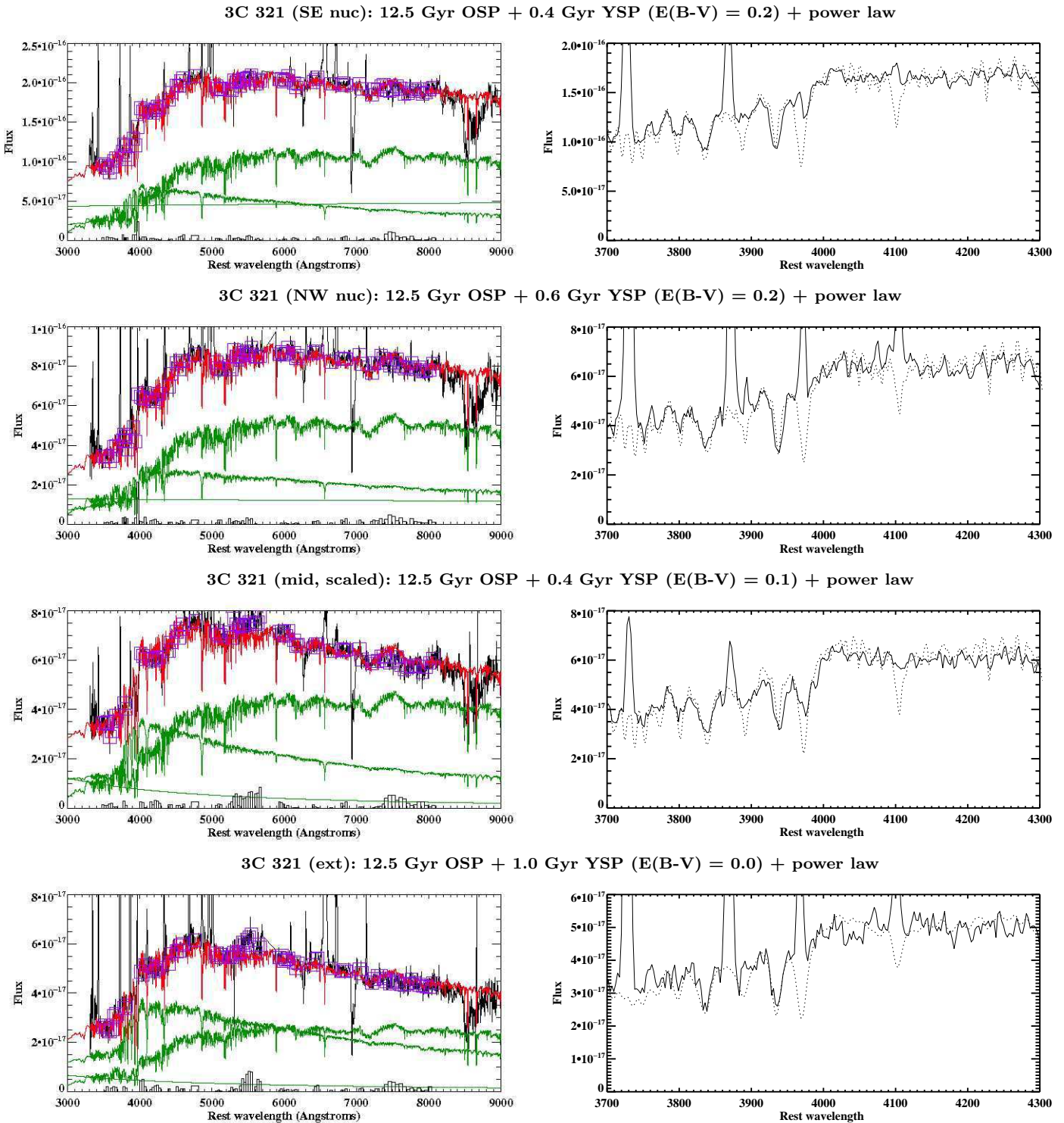


**Figure 5.** Detection of a broad component to H $\alpha$  in the nuclear aperture of 3C 381 with FWZI  $\sim 300\text{\AA}$  or  $\sim 14,000$  km s $^{-1}$ . The lines plotted are: nebular continuum subtracted nuclear spectrum (bold solid line; offset by  $-0.4 \times 10^{-16}$  erg s $^{-1}$  cm $^{-2}$   $\text{\AA}^{-1}$ ), best fitting (OSP+power law; offset by  $-0.4 \times 10^{-16}$  erg s $^{-1}$  cm $^{-2}$   $\text{\AA}^{-1}$ ) SED model (solid line) and the continuum (OSP+power law) subtracted nuclear spectrum (dotted line). Note, the spectrum has not been corrected for atmospheric absorption features and the A band (at  $\sim 7600$   $\text{\AA}$ ) is coincident with the H $\alpha$ /[N II] blend in the observed frame.

ion (de Koff et al. 1996; Roche & Eales 2000). Although Grandi & Osterbrock (1978) reported the detection of weak broad wings to H $\alpha$  along with high ionization narrow lines, Dennett-Thorpe et al. (2000) & Eracleous & Halpen (2004) failed to find evidence for broad H $\alpha$  in their higher S/N spectra. Moreover, Dennett-Thorpe et al. (2000) argue against the classification of this object as a BLRG because the radio core and jet are relatively weak, and the near-IR colours are consistent with NLRGs rather than BLRGs (c.f. Lilly & Longair 1982). Rudy et al. (1983) measure a relatively low polarisation for 3C 381 at optical wavelengths:  $1.8 \pm 0.6\%$ , consistent with the observations of other BLRGs in their sample. On the basis of Figure 1, 3C 381 has a clear UV excess. Given that it is only marginally resolved (Figure 1), we have extracted only a nuclear aperture for this source.

We find that an adequate fit to the SED and the discrete features can be obtained using a two component (OSP plus power-law) model ( $\chi_{\text{red}}^2 = 0.90$ ) where 80% and 20% of the flux originates from the OSP and power-law respectively. This model is shown in Figure 4. In this model, the power-law component is red ( $\alpha = 1.65$ ) which suggests that, if the light originates from the AGN, it is direct rather than scattered, consistent with the low optical polarisation.

In Figures 4 and 5 there is clear evidence for a broad component to H $\alpha$  in the form of an excess in the continuum region around H $\alpha$  relative to our best fitting model. This excess has a FWZI of  $\sim 300\text{\AA}$  or  $\sim 14,000$  km s $^{-1}$ . However, due to the strong atmospheric A band ( $\sim 7600\text{\AA}$ ) coincident with the H $\alpha$ /[N II] blend, it is not possible to model this component in detail. We further note that, although Chiaberge et al. (2002) present only an upper limit on the flux of a compact nucleus in this source based on HST images, their upper limiting flux is consistent with the flux in the power-law component required by our continuum mod-

Figure 4. SEDs and detailed fits *continued*

elling. Hence, our observations are consistent with a BLRG classification for 3C 381.

Despite the possible evidence for a broad line nucleus in this object, the evidence is not conclusive. Therefore, we have modelled the SED including a YSP, both with and without a power-law component. Figure 3 shows the  $\chi^2_{\text{red}}$  space for the OSP plus YSP models. For the two com-

ponent models, we find one minimum ( $\chi^2_{\text{red}} = 0.85$ ) for an OSP plus a 0.02 Gyr YSP reddened by  $E(B-V) = 1.0$  contributing 82% and 17% of the flux in the normalising bin respectively. This model also produces a viable fit to the stellar absorption lines.



#### 4.3.6 3C 433

The FR I/FR II radio galaxy 3C 433 is peculiar at both radio and optical wavelengths. The radio source extends over  $\sim 100$  kpc and is highly asymmetric in both the strength and shape of the radio emission, overall resembling an ‘x’ shape (e.g. van Breugel et al. 1983; Black et al. 1992). Such complex radio morphology, often associated with lower power radio sources, is unexpected due to the relatively high power of the radio source (van Breugel et al. 1983).

Optically, 3C 433 is identified with a NLRG (Koski 1978), with a bright companion galaxy  $\sim 10$  arcsec to the NE (van Breugel et al. 1983; Baum et al. 1988), and the nuclei of both galaxies are surrounded by a common envelope (Matthews & Morgan 1964). A fainter galaxy is observed  $\sim 25$  arcsec to the SW. The large-scale optical structure is complex, with emission line filaments clearly detected in ground-based ( $H\alpha$ ) images (e.g. Baum et al. 1988; McCarthy et al. 1995), and patchy dust features, some trailing in the direction of the radio jet, also detected in higher resolution HST images (de Koff et al. 2000).

Modelling of the spectrum of the SW nucleus by Wills et al. (2002) suggests that the large UV excess observed is attributable to a significant ( $\sim 20$ -40% contribution to the flux at  $4780\text{\AA}$ ), highly reddened ( $E(B-V) \sim 0.5$ -0.7) YSP (0.05-0.1 Gyr). Note that, on the basis of the lack of a broad component to  $H\alpha$  and the low UV polarisation ( $< 8\%$ ; Wills et al. 2002), reddened YSP models are favoured over scattered AGN models for this source. Moreover, while this object shows unusually red colours at near-IR wavelengths (Lilly et al. 1985), and a relatively high surface brightness in the complex nuclear structure revealed by the optical HST images, the nucleus is resolved and there is no evidence for a point source at optical wavelengths (Chiaberge, Capetti & Celotti 1999).

In our new WHT observations the slit position was chosen to cover both nuclei. We find that the UV excess covers the entire measureable extent of the double nucleus system (see Figure 1). Hence, we have extracted three apertures: one for the SW nucleus coincident with the radio source, one for the NE nucleus, and one sampling the region between the nuclei. All apertures are shown on Figure 1.

**The SW nucleus.** The SW nucleus of the 3C 433 system, coincident with the main radio source, is likely to have a YSP component (see Wills et al. 2002). However, it is possible to obtain a marginally acceptable fit ( $\chi_{\text{red}}^2 = 1.40$ ) to the SED and absorption features using an OSP (74%) plus a power-law component (24%;  $\alpha = 1.0$ ) only, consistent with the two component fitting by Wills et al. (2002). Since the UV polarisation is low ( $< 8\%$ ; Wills et al. 2002), the large power-law is unlikely to be due to a scattered AGN component. Although the fitted power-law is red, which might be consistent with a direct AGN component, given the failure to detect a point source in broad-band HST images (Chiaberge et al. 1999) and broad wings to the  $H\alpha$  in our spectra, an interpretation in terms of a highly reddened YSP component is more plausible.

Figure 3 shows the plot of the  $\chi_{\text{red}}^2$  space for models that only include YSP and OSP components. Wills et al. (2002) found a two component OSP plus YSP model gave as good or better fits than an OSP plus a power-law and the results presented here are consistent with this – there is a

clear minimum in the  $\chi_{\text{red}}^2$  space at YSP age  $\sim 0.05$  Gyr with reddening  $E(B-V) \sim 0.7$  and  $\chi_{\text{red}}^2 \sim 0.6$  contributing  $\sim 20$ -30% of the flux in the normalising bin. Models with YSP ages greater than 0.2 Gyr are ruled out by our SED modelling. An example of a two component model is shown in Figure 4 with: 12.5 Gyr OSP (67%) plus 0.05 Gyr YSP ( $E(B-V) = 0.7$ , 32%) with  $\chi_{\text{red}}^2 = 0.6$ . It is clear that this model also provides an acceptable fit to the stellar absorption features.

**The NE nucleus.** The SED of the NE nucleus is markedly different to that of the active SW nucleus – the  $4000\text{\AA}$  break is more prominent, as are the stellar absorption features (e.g. CaII H+K), whilst there is little evidence for line emission. However, it is possible to model the SED with an OSP, both with and without a power law ( $\chi_{\text{red}}^2 = 0.99$  and 1.1 respectively). Figure 4 shows the OSP (100%) model.

Despite being able to model the SED adequately without a YSP component, because there is evidence for a significant UV excess (see Figure 1), we have attempted to model the SED including a YSP to see how the fit will change. In the two component OSP plus YSP models, the SED fit improves significantly when including a YSP and good fits ( $\chi_{\text{red}}^2 < 1$ ) are obtained for all ages of YSP (see Figure 3). The inclusion of the YSP component also improves the fit to the absorption lines, although the younger ( $\lesssim 0.03$ ) and older ( $\gtrsim 1.6$ ) ages tend to over predict some of the absorption features. An example of the 12.5 Gyr OSP (89%) plus a 0.1 Gyr YSP ( $E(B-V) = 0.8$ , 10%) with  $\chi_{\text{red}}^2 = 0.57$  is shown in Figure 4. Despite the fact that the models are virtually indistinguishable, all consistently have OSP and YSP contributions of 95-65% and 5-30% respectively with  $\chi_{\text{red}}^2 \sim 0.45$ -0.9.

**Between the nuclei.** As highlighted in Figure 1, the UV excess is spatially resolved and extends across the entire system, with a similar  $D4000$  ratio. We have therefore also investigated an aperture located between the two nuclei. The location of this aperture is shown on Figure 1.

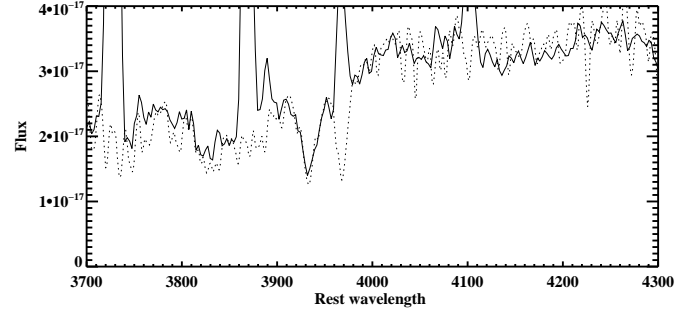
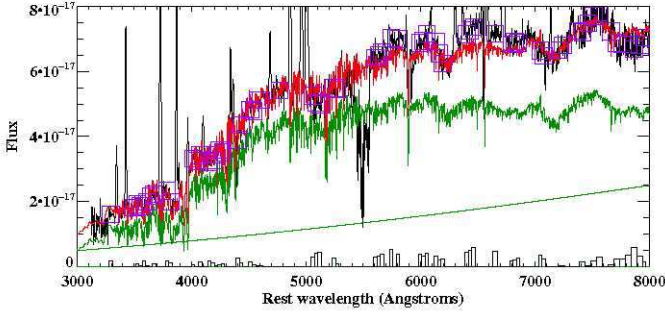
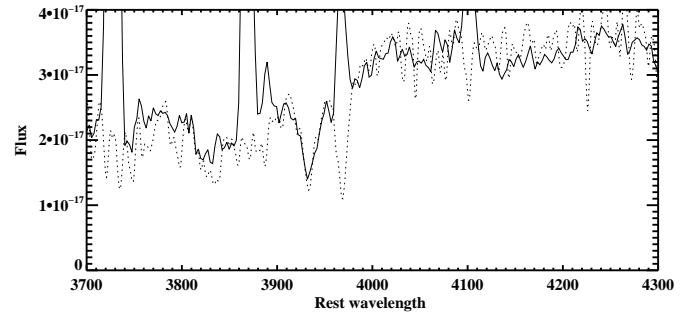
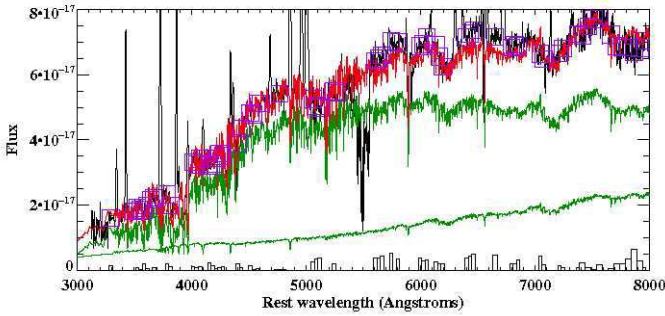
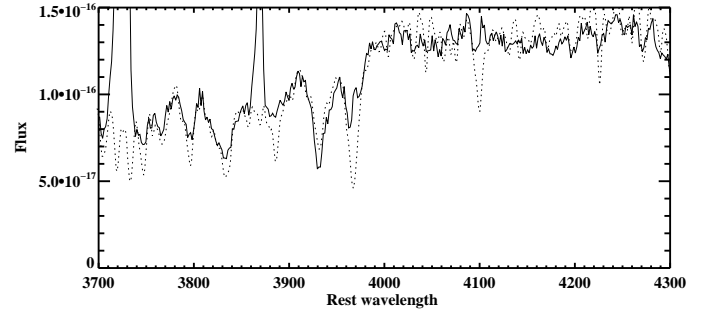
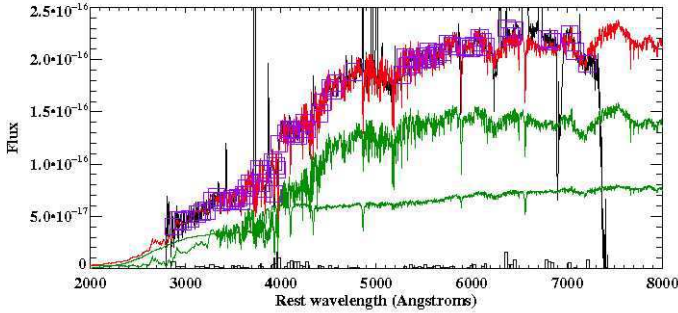
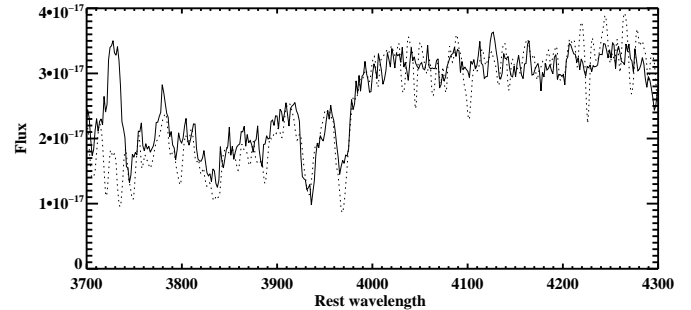
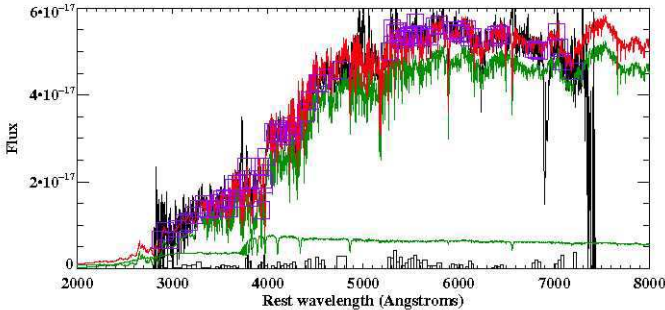
It is not possible to model this aperture with an OSP alone, with or without a power-law component. Moreover, an AGN component is not expected in this aperture as it is located far from the active nucleus and does not contain any line emission – the UV excess is therefore likely to be due to a population of young stars.

Figure 3 shows the  $\chi_{\text{red}}^2$  space for two component OSP plus YSP models. Two minima are clearly seen at  $\sim 0.1$ -0.2 Gyr ( $E(B-V) \sim 0.5$ ) and  $\sim 1$ -2 Gyr ( $E(B-V) \sim 0.2$ ) – note that viable fits are also found between the minima. As for other apertures displaying such a degeneracy in the fits, we can rule out older age YSPs on the basis of the strength of CaII K – models including YSPs older than  $\sim 1.0$  Gyr significantly over-predict the strength of CaII K. For all models in this range, the OSP and YSP contributions are typically 80-95% and 10-25% respectively with  $E(B-V) \sim 0$ -0.7. Figure 4 shows an example of a good fitting model: 12.5 Gyr OSP (91%) plus 0.1 Gyr YSP ( $E(B-V) = 0.5$ , 15%) with  $\chi_{\text{red}}^2 = 0.95$ .

#### 4.3.7 PKS 0023-26

The powerful ( $\log P_{5\text{GHz}} = 27.33$  W Hz $^{-1}$ ) Compact Steep Spectrum (CSS) radio source PKS 0023-26 is iden-

3C 381: 12.5 Gyr OSP + power law

3C 381: 12.5 Gyr OSP + 0.02 Gyr YSP ( $E(B-V) = 1.0$ )3C 433 (SW nuc): 12.5 Gyr OSP + 0.05 Gyr YSP ( $E(B-V) = 0.7$ )3C 433 (mid): 12.5 Gyr OSP + 0.1 Gyr YSP ( $E(B-V) = 0.5$ )Figure 4. SEDs and detailed fits *continued*

tified with an  $m_v = 19.5$  galaxy (Prestage & Peacock 1983; Wall & Peacock 1985). The double lobed radio source has a maximum size of  $\sim 680$  mas ( $\sim 4.25$  kpc), aligned along PA  $-34$  (Tzioumis et al. 2002). Spectroscopically it is classified as an NLRG and its emission line spectrum has intermediate ionisation with relatively strong  $[\text{O II}]\lambda\lambda 3727$  and  $[\text{N I}]\lambda 5199$  emission (Tadhunter et al. 1993; Morganti et al.

1997). The optical continuum displays a large UV excess with low UV polarisation ( $P_{UV} < 2.0\%$ ) and no sign of broad permitted lines. This source is therefore a possible starburst candidate (Tadhunter et al. 1993; Morganti et al. 1997; Tadhunter et al. 2002).

Figure 1 shows that the UV excess is extended beyond the immediate nuclear regions (indicated in figure). We were

unable to obtain adequate fits to the spectrum of the nuclear aperture of PKS 0023-26 with an OSP alone or an OSP plus power-law component. Indeed, the spectrum shows clear evidence for the high order Balmer lines in absorption (see Figure 4).

For models including an OSP and a YSP we find a clear minimum in the  $\chi_{\text{red}}^2$  space for a young YSP age ( $\sim 0.03$ - $0.05$  Gyr) with significant reddening ( $E(B-V) \sim 0.8$ ) and a  $\sim 50$ - $60\%$  contribution from the YSP component (see Figure 3). Detailed comparisons for this aperture are difficult as many of the absorption features are infilled by strong emission lines. However, the CaII K line is not filled and on the basis of the fit to CaII K and the surrounding continuum, the best fitting model is for an OSP plus a young (0.03 Gyr) YSP with significant reddening ( $E(B-V) = 0.9$ ); this model is shown in Figure 4: 12.5 Gyr (44%) plus YSP (0.03 Gyr,  $E(B-V) = 0.9$ , 54%) with  $\chi_{\text{red}}^2 = 1.1$ . Models including older age YSPs fail to reproduce the continuum in this region and, as the age increases, the CaII K line is over-estimated.

As for many of the other objects/apertures, including a power-law component significantly increases the range of viable YSP fits. A single broad minimum is observed covering a large range of YSP ages (0.05-2.0 Gyr) and reddenings ( $E(B-V) \lesssim 1.2$ ). YSP models within this minimum are indistinguishable due to the power law contribution (10-60%). However, previous studies of PKS 0023-26 have found that, whilst the UV excess is large, there is little evidence for a significant AGN component – no broad permitted lines are observed (making a significant direct component unlikely, Tadhunter et al. 2002 and this paper) and the UV polarisation is low, ruling out a large scattered component (Tadhunter et al. 2002).

It is encouraging to note that all of the better fits including a power-law component require at least 20% of the flux to originate from the YSP, often as high as 50%, although the dominance of the power law component for some models make distinguishing between the ages in the three component models difficult.

#### 4.3.8 PKS 0039-44

PKS 0039-44 is one of the higher redshift sources in our sample ( $z = 0.346$ ) and has been previously studied as part of the 2Jy survey by Tadhunter et al. (e.g. Tadhunter et al. 1993, 2002). This FR-II double-lobed radio source is identified with a galaxy displaying a rich, high ionisation emission line spectrum (Tadhunter et al. 1993) and is classified as an NLRG.

PKS 0039-44 shows evidence for a significant UV excess (see Figure 1) and Tadhunter et al. (2002) have previously investigated the optical/UV continuum using lower resolution data and spectral synthesis models. Whilst their observations show PKS 0039-44 to be significantly polarised ( $P_{UV} = 4.8 \pm 1.2\%$ ), suggesting a scattered AGN component is likely to be significant, Tadhunter et al. (2002) believe this component is not necessarily the *dominant* component in the UV. This is because the *intrinsic* polarisation of the continuum component causing the UV excess is relatively low ( $P_{UV} < 10\%$ ), and they detected no broad emission lines. Tadhunter et al. therefore believe that PKS 0039-44 is a good candidate for a significant contribution from a YSP.

Tadhunter et al. (2002) also report a 19% contribution of the nebular continuum in the UV.

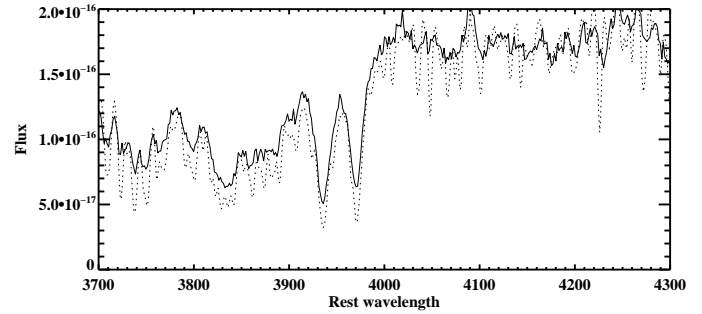
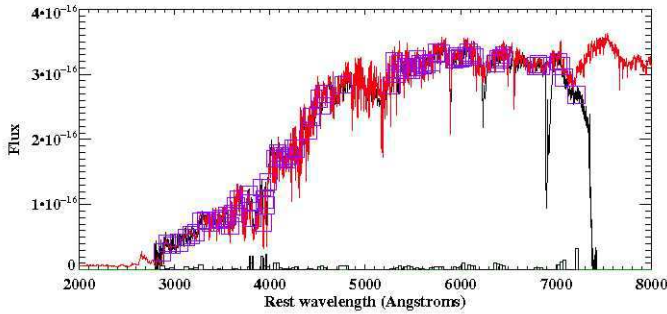
As found by Tadhunter et al. (2002), we can adequately model the SED using an OSP and a power-law component ( $\chi_{\text{red}}^2 = 0.4$ ) contributing 57 and 40% to the flux in the normalising bin respectively. As well as reproducing the SED, this fit also provides an adequate fit to the stellar absorption features, and the slope of the required power-law ( $\alpha \sim -0.5$ ) is consistent with a scattered AGN component. Further evidence for a scattered AGN component is provided by the clear detection of a broad MgII feature (FWHM  $\sim 9000$  km  $s^{-1}$ : see Figure 6).

Although the detection of significant UV polarisation and a broad MgII feature suggest a major contribution from a scattered AGN component, this does not by itself rule out a significant contribution from a YSP component. Hence, we have modelled the SED including both YSP and power-law components. Unsurprisingly, given the contribution of the scattered AGN, the models do not provide strong constraints on the age of the YSP: *all* ages of YSP provide a viable fit to the SED ( $\chi_{\text{red}}^2 \lesssim 0.4$ ) and the detailed fits to the absorption lines are indistinguishable. However, by comparing the percentage contributions of the components, some models can be ruled out if it is assumed that both a YSP and a power-law are required – many of the viable fits do not require a YSP component (0% model contribution). Ruling these out, all of the results are broadly consistent with component contributions of  $\sim 20$ - $50\%$ ,  $\sim \text{few}$ - $20\%$  and  $25$ - $40\%$  for the OSP, YSP and power-law ( $-0.7 < \alpha < -0.2$ ) respectively. However, the this only rules out certain regions of the *reddening* space ( $E(B-V) < 1.0$  with larger reddenings required for younger YSPs) and viable models are still obtained for all ages of YSP. Overall, while the optical continuum of PKS 0039-44 clearly has a large contribution from a scattered AGN component, we cannot rule out a significant contribution from a YSP component. Indeed, such a component would help to explain the fact that the UV polarisation is lower than expected if the UV excess is solely due to scattered AGN light (Tadhunter et al. 2002).

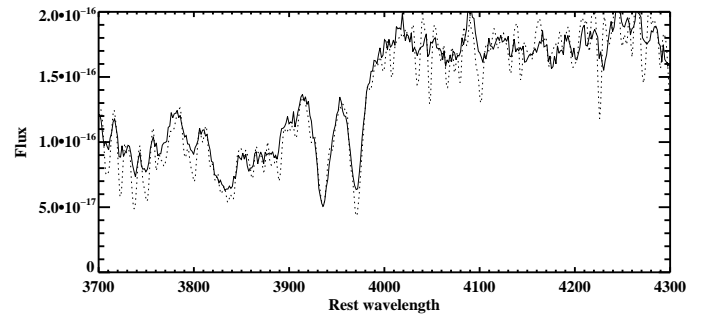
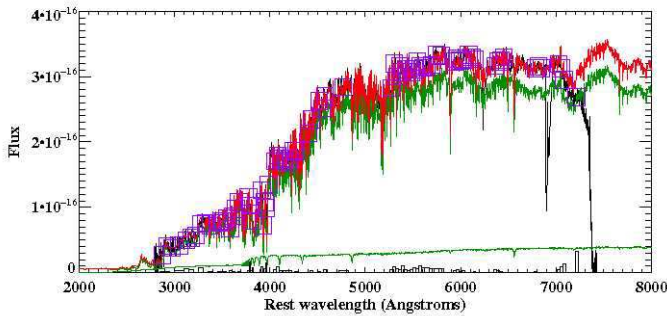
PKS 0039-44 is one of the higher redshift objects in our sample ( $z = 0.346$ ). Therefore we have further modelled the SED using different OSPs in addition to the ‘standard’ 12.5 Gyr population used for the majority of the sources in the sample. Based on the redshift, a Hubble constant of  $75$  km  $s^{-1}$  Mpc $^{-1}$  gives ages of the universe at the source redshift between 10.5 and 13 Gyr for an open and flat universe respectively. We have therefore also modelled the data with an OSP of age 10 Gyr. This gives similar results (50-55% old, 40-45% power-law with  $0.4 < \alpha < 0.5$ ) to models with a 12.5 Gyr OSP. Therefore we conclude that, given the large contribution of the power-law and/or YSP components, our modelling does not provide strong constraints on the age of the OSP component.

Because the SED of PKS 0039-44 can be adequately modelled by an OSP and a power-law component and there is the hint of a possible broad component to Mg II, we do not show a contour plot for the YSP models. As an example of the fits obtained, we show the model comprising an OSP and a power-law component with the best chi-squared, comprising a 10Gyr OSP (57%) and a power-law component (41%;  $\alpha = -0.5$ ) in Figure 4.

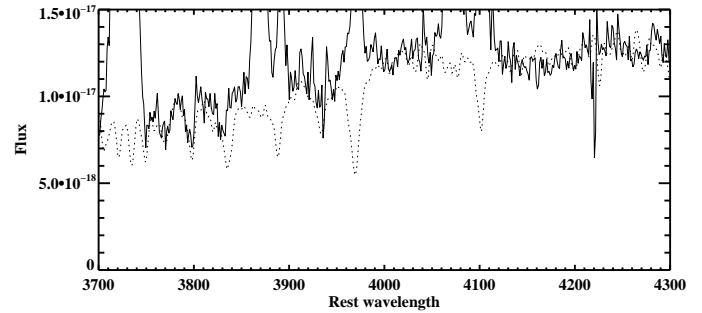
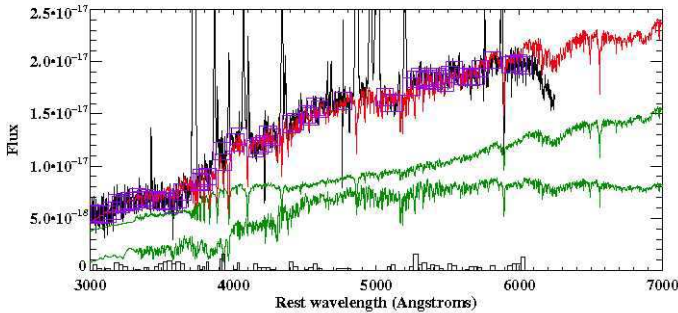
3C 433 (NE nuc): 12.5 Gyr OSP



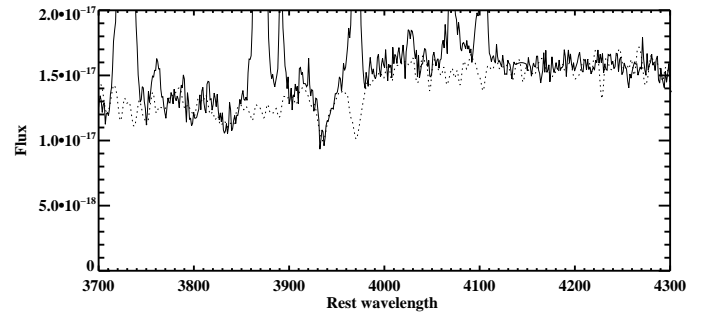
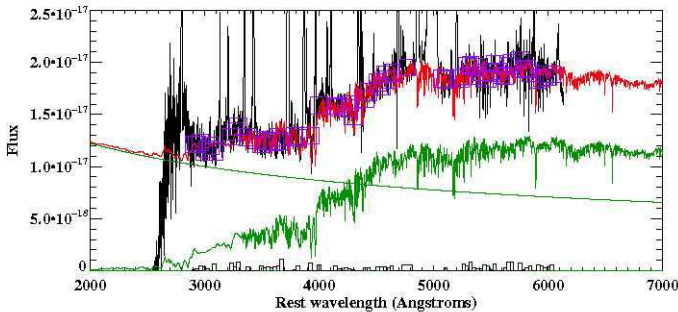
3C 433 (NE nuc): 12.5 Gyr OSP + 0.1 Gyr YSP (E(B-V) = 0.8)



PKS 0023-26: 12.5 Gyr OSP + 0.03 Gyr YSP (E(B-V) = 0.9)



PKS 0039-44: 10 Gyr OSP + power law

Figure 4. SEDs and detailed fits *continued*

#### 4.3.9 PKS 0409-75

At  $z = 0.693$ , PKS 0409-75 is both the most distant radio source in our sample and the most powerful at radio wavelengths. Indeed, it is one of the most powerful intermediate redshift radio sources in the southern hemisphere ( $L_{45\text{MHz}-4.8\text{GHz}} = 10^{45.19} \text{ erg s}^{-1}$ ; Alvarez et al. 1993). The FR II radio source is relatively small (LAS = 9 arcsec or 85

kpc) and is dominated by two lobes of emission extending along PA130 (Morganti et al. 1999). PKS 0409-75 is optically identified with an  $m_V = 21.6$  galaxy which is possibly resolved into two components and displays extended emission in  $[\text{O II}]\lambda\lambda 3727$  (di Serego Alighieri et al. 1994). Low resolution optical spectra of PKS 0409-75 reveal a significant UV excess compared with passively evolving elliptical

galaxies at similar redshifts (Tadhunter et al. 2002). This is also highlighted in our new measurements shown in Figure 1. The narrow emission line luminosity and ionisation state are relatively low for the radio power – [O III] is barely detected whilst [O II] is relatively strong in the spectrum presented by Tadhunter et al. (1993). Tadhunter et al. (2002) attempted to model the optical/UV continuum but were unable to obtain a result due to poor sky subtraction. They do report a measurement of the 4000Å break which suggests 95% of the light in the 3750-3950Å region is not emitted by the OSP. Further, due to the low UV polarisation ( $P_{UV} < 6.3\%$ ) and non-detection of broad permitted lines in the UV spectrum (e.g. Mg II), Tadhunter et al. propose PKS 0409-75 to be a strong starburst candidate.

By using the VLT and paying careful attention to the calibrations and sky subtraction, we have obtained new deep, higher resolution optical spectra of PKS 0409-75 which are of sufficient quality to model the SED. Using the simplest models, we find the SED shape can be adequately modelled using an OSP and a power-law component. As for PKS 0039-44, we have also considered OSP ages younger than 12.5 Gyr and find the best fitting model is for a 7 Gyr OSP plus a power-law component ( $\chi_{\text{red}}^2 = 1.2$ ), each contributing 60 and 45% of the flux in the normalising bin respectively. This fit is shown in Figure 4.

However, whilst an adequate fit can be gained without a YSP component, no significant polarisation has been detected for this source in the UV (Tadhunter et al. 2002), the required power-law spectral index is relatively red ( $\alpha \sim 0.86$ ), no broad permitted lines have been detected, and the emission line luminosity is relatively low. Together, these features make a major contribution from a scattered AGN component unlikely, although without high resolution HST imaging we cannot absolutely rule out a contribution from a direct AGN component.

Given the lack of clear evidence for an AGN contribution to the UV excess, we have also attempted to model the SED of PKS 0409-75 including a YSP component.

For models with an OSP (7 Gyr) and a YSP only, viable fits can be obtained with a young ( $< 0.04$  Gyr), reddened ( $E(B-V) \sim 0.8$ ) YSP contributing  $\sim 25$ -45% of the flux in the normalising bin. Figure 3 shows the  $\chi_{\text{red}}^2$  space for models including an OSP and a YSP and Figure 4 shows an example of a good fitting two component model: 7 Gyr OSP (73%) plus 0.02 Gyr YSP ( $E(B-V) = 0.7$ ; 32%) with  $\chi_{\text{red}}^2 = 0.75$ ). Inspection of the detailed fits shows that, due to the noise in the data, all of the models close to the  $\chi_{\text{red}}^2$  minimum provide good fits to the absorption features and are indistinguishable.

#### 4.3.10 PKS 1932-46

The double-lobed FR II radio source PKS 1932-46 is optically identified with an early-type galaxy at  $z = 0.231$  located between the two radio lobes but closest to the eastern lobe (di Serego Alighieri et al. 1994). The galaxy has a double structure in [O III] emission with the two components separated by 5 arcsec (25 kpc). The SW component is coincident with the optical continuum emission. The main galaxy structure is surrounded by a giant (up to  $\sim 160$  kpc) emission line nebula, making this one of the largest emission line haloes ever detected around an ac-

tive galaxy at any redshift (Villar-Martín et al. 1998, 2005). Note, Villar-Martín et al. (2005) used the same data set presented in this paper. The halo is complex in structure with clumps and filaments of emission and evidence for stellar photoionization of the emission line regions on scales of more than 100 kpc in a direction close to perpendicular to the radio axis (Villar-Martín et al. 2005). The nuclear spectrum shows a clear UV excess (Tadhunter et al. 2002; see also Figure 1), and a rich emission line spectrum with moderate ionisation (Tadhunter et al. 1993; Villar-Martín et al. 2005). The detection of weak broad permitted lines (FWHM  $\sim 2400$  km s $^{-1}$ ) was reported by Villar-Martín et al. (1998) although Villar-Martín et al. (2005) retracted this detection after analyses of higher quality data showed H $\alpha$  could be modelled by the same kinematic components as [O III] $\lambda\lambda 4959, 5007$ . Tadhunter et al. (2002) have modelled a lower resolution spectrum of the nuclear regions and suggest that, in addition to an OSP and power-law component, a contribution from a YSP is also likely. PKS 1932-46 is not significantly polarised in the UV ( $P_{UV} < 1.6\%$ ; Dickson 1997; Tadhunter et al. 2002).

We find that it is possible to model the nuclear SED of PKS 1932-46 adequately with an OSP and a flat ( $\alpha = 0.23$ ) power-law component ( $\chi_{\text{red}}^2 = 0.82$ ) with 59% and 41% of the flux in the normalising bin originating in the two components respectively. The best fitting model is shown in Figure 4.

Given that the UV polarisation is low (Tadhunter et al. 2002) and the modelled power-law component is red, this suggests that any light originating from the AGN will be direct. The best (ground-based) images of PKS 1932-46 known to us are presented in Villar-Martín et al. (1998) and are of insufficient resolution to determine whether a strong point source is detected. However, further evidence for or against a significant AGN contribution can be gained from the detection/non-detection of broad permitted lines. As discussed above, previous searches for broad lines in the nuclear spectrum give contradictory results. After subtracting off the best fitting model (12.5 Gyr OSP plus power-law), we find evidence for a broad component to H $\alpha$  (see Figure 7) although this component is significantly broader (FWHM  $\sim 5100$  km s $^{-1}$ ) than the original detection (FWHM  $\sim 2400$  km s $^{-1}$ ). Whilst Villar-Martín et al. (2005) used the same spectra as presented here and searched for such a broad component, due to its broadness their non-detection is not surprising for a number of reasons. First, although the flux in the component is relatively large, the large FWHM reduces the peak flux to the point that it is only clear when a large spectral range is studied. Second, analysis in the Villar-Martín et al. (2005) paper focussed on a region around H $\alpha$  only 250Å wide in the observed frame whilst the component detected here has FWHM  $\sim 140$ Å and a total width of  $\sim 370$ Å in the observed frame. Finally, Villar-Martín et al. (2005) did not model and subtract the continuum – a step which has been shown to be vital for studying the broader emission line components in radio galaxies (e.g. in PKS 1345+12; Holt et al. 2003). We therefore support the classification of PKS 1932-46 as a BLRG.

Given the strong evidence for broad lines in the nuclear spectrum of PKS 1932-46 it is likely that a direct AGN component makes a major contribution to the optical/UV continuum. However, there is strong evidence from the HII-

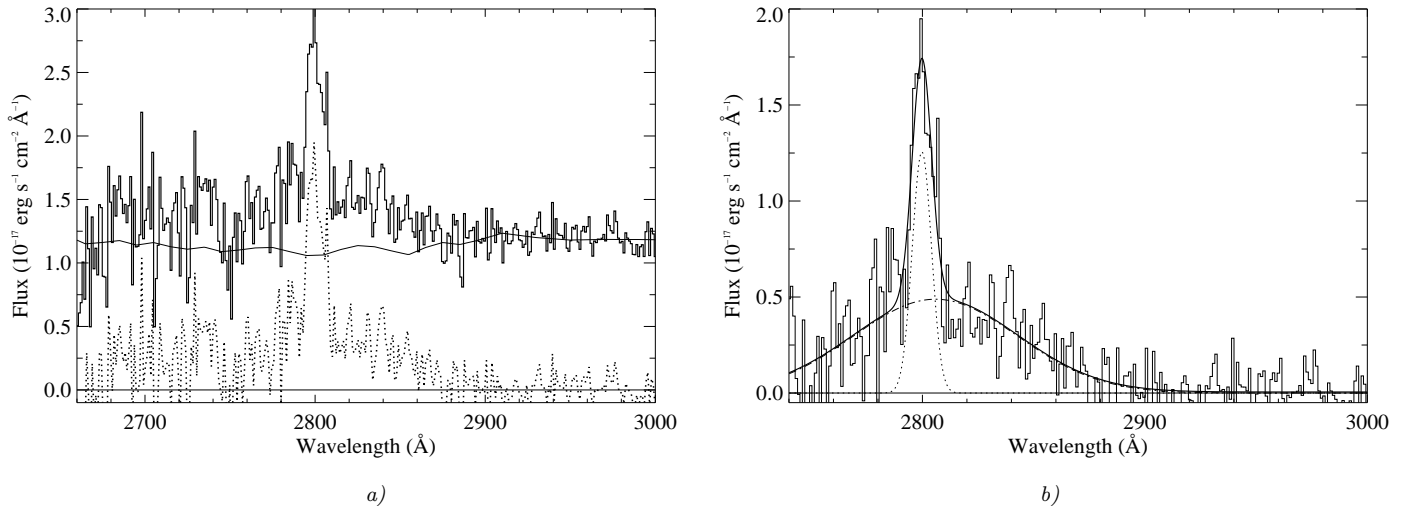


**Figure 6.** Detection of a broad component to Mg II in the nuclear aperture of PKS 0039-44. *a)* Plot showing a zoomed in region of the nuclear spectrum of PKS 0039-44 highlighting the underlying broad component to Mg II. The lines plotted are: nebular continuum subtracted nuclear spectrum (bold solid line), best fitting (OSP+YSP+power law) SED model (solid line) and the continuum (OSP+YSP+power law) subtracted nuclear spectrum (dotted line). In plot *b)* we model the emission line components of the Mg II blend. The 2 component model comprises an intermediate ( $\sim 1100 \text{ km s}^{-1}$ ) component (dotted lines) and a broad ( $\sim 9300 \text{ km s}^{-1}$ ) component (dashed lines).

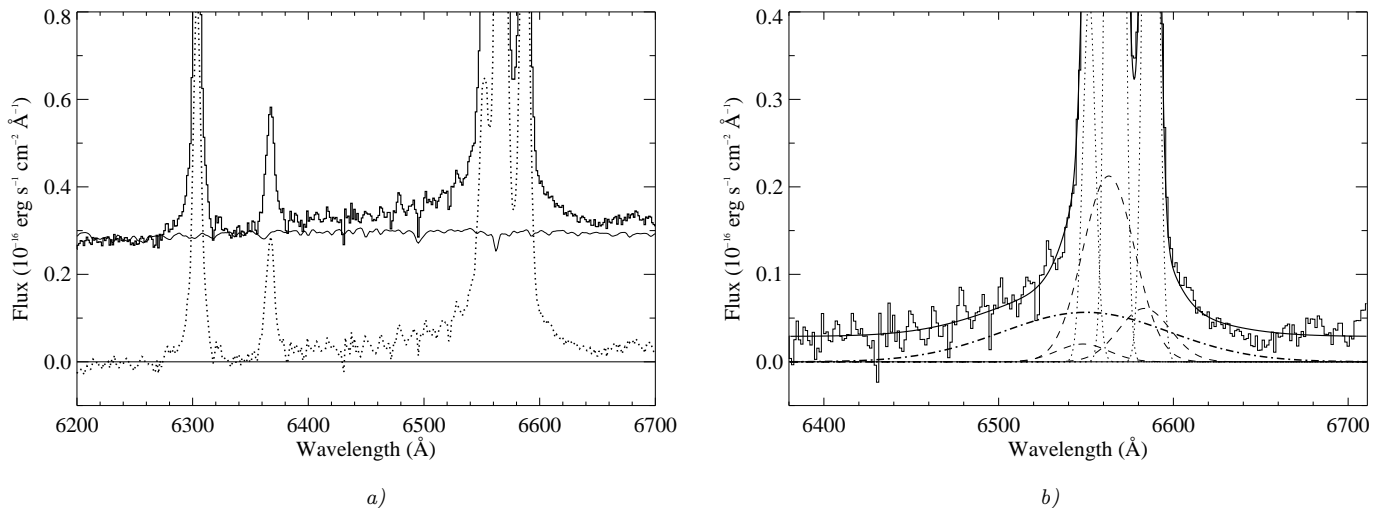


**Figure 7.** Detection of a broad component to the emission lines in the nuclear aperture of PKS 1932-46. *a)* Plot showing a zoomed in region of the nuclear spectrum of PKS 1932-46 highlighting the underlying broad component to H $\alpha$ . The lines plotted are: nebular continuum subtracted nuclear spectrum (bold solid line), best fitting (OSP+power-law) SED model (solid line) and the continuum (OSP+power-law) subtracted nuclear spectrum (dotted line). In plot *b)* we model the emission line components of the H $\alpha$ /[N II] blend. The 7 component model comprises a narrow ( $180 \text{ km s}^{-1}$ ) component (dotted lines) and a broad ( $1550 \text{ km s}^{-1}$ ) component (dashed lines) to both H $\alpha$  and the [N II] $\lambda\lambda 6548, 6583$  doublet, and a further very broad ( $5130 \text{ km s}^{-1}$ ) component (dot-dashed line) to H $\alpha$ .

region like emission line ratios for ongoing star formation in the extended halo of this object (Villar-Martín et al. 2005). Moreover, when fitting a two component model (OSP plus power-law), Tadhunter et al. (2002) remained confident that a YSP component was required after the subtraction of their model left significant residuals. Indeed, detailed inspection of the SED in the region  $\sim 3700\text{--}4100\text{Å}$  reveals a narrow absorption line at  $\sim 3830\text{Å}$ —most likely H9  $\lambda 3835$ . Whilst the two component (OSP plus power-law) model reproduces the majority of the SED well, it fails to provide a good fit to

this feature. Hence we have also attempted to model the SED using a three component fit (as the evidence suggests a significant AGN component is required) to include a YSP; the plot of the  $\chi^2_{\text{red}}$  space is shown in Figure 3. Unsurprisingly, the three component models produce viable fits for all ages of YSP with a large minimum in the range 0.05–3.0 Gyr with  $E(B-V) \lesssim 0.8$  and it is virtually impossible to distinguish between these models. However, it is clear that a YSP component is required to model the H9 line. The models have varying contributions from the three components:

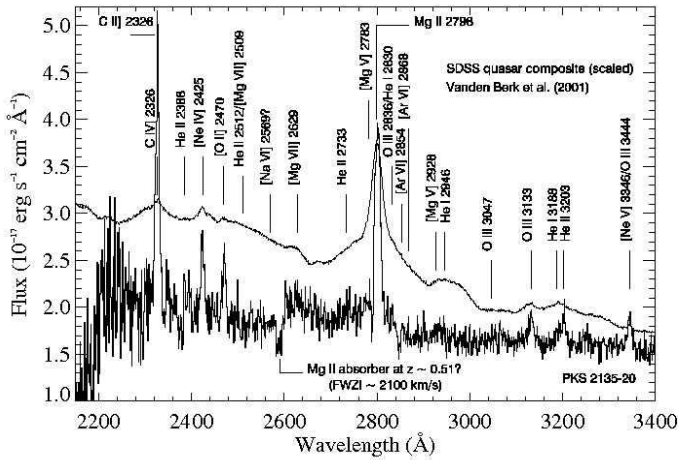


**Figure 8.** Identification of the features in the nuclear aperture of PKS 2135-20 in the UV in the range 2200-3400Å. Line IDs are taken from Tran et al. (1998). The nebular continuum subtracted spectrum of the nuclear aperture of PKS 2135-20 is plotted along with a scaled version of the SDSS quasar template taken from Vanden Berk et al. (2001) and line identifications for the known emission lines in this region. From this, it seems likely that the broad feature at  $\sim 2600$ -2700Å is the result of several different emission line components, namely a broad component to Mg II  $\lambda 2798$  plus emission from He II  $\lambda 2734$  and [Mg VII]  $\lambda 2632$ . The dip observed in the spectrum of PKS 2135-20 at  $\sim 2600$ Å, which is not observed in the quasar template spectrum, is possibly at least partially caused by the combination of the quasar with the light from the stellar populations – there is a small ‘break’ in all of the stellar templates at  $\sim 2600$ Å present which appears stronger for older age populations.

$\sim 0$ -60% OSP,  $\sim 10$ -80% YSP and  $\sim 5$ -40% power-law with  $\alpha \gtrsim -0.6$ . Including the YSP improves the fit to H9, with the marginally better fits for the younger age YSPs suggesting that a YSP component may be important on the 10-20% level in the normalising bin. In addition to the OSP plus power-law fit, we also show an example of a three component model in Figure 4: 12.5 Gyr (54%) plus a 0.05 Gyr YSP (19%;  $E(B-V) = 0.4$ ) and a power-law component (28%;  $\alpha = 0.9$ ). This model has a  $\chi^2_{\text{red}}$  of 0.44.

#### 4.3.11 PKS 2135-20

The powerful ( $\log P_{5\text{GHz}} = 27.47 \text{ W Hz}^{-1}$ ) Compact Steep Spectrum (CSS) radio source PKS 2135-20 is identified with an  $m_V = 19.4$  galaxy (Wall & Peacock 1985) at redshift  $z = 0.635$  (di Serego Alighieri et al. 1994) and has the second highest redshift in our sample. At radio wavelengths, the MERLIN 5 GHz image shows a double-lobed, highly asymmetric structure covering  $\sim 250$  mas ( $\sim 3$  kpc) along PA 52 (Tzioumis et al. 2002). All of the radio flux is detected in the MERLIN image suggesting there are no extended components.

Broad-band imaging of PKS 2135-20 by Shaw et al. (1995) reveals a compact structure, while spectra and polarisation measurements demonstrate that this object has a large UV excess combined with a low UV polarisation ( $P_{UV} < 2.7\%$ ; Tadhunter et al. 2002). Moreover, Shaw et al. (1995) and Tadhunter et al. (2002) report the detection of

high order Balmer lines in absorption, consistent with the presence of a significant YSP component.

Spectroscopically, the classification of the AGN component in PKS 2135-20 is uncertain. Originally classified as an NLRG on the basis of its rich spectrum of narrow emission lines with moderate ionisation (e.g. Tadhunter et al. 1993), deep EFOSS spectra reveal evidence for broad permitted lines (e.g. MgII, H $\beta$ ) suggesting PKS 2135-20 is instead a BLRG (Shaw et al. 1995). Further, the relatively low UV polarisation of the source suggests that we are detecting direct rather than scattered AGN light. Similarly, the classification of PKS 2135-20 as a radio galaxy has been brought into question by Tadhunter et al. (1998) who suggest that its absolute magnitude of  $M_V < -23.0$  is consistent with the classification of PKS 2135-20 as a QSO using the criteria of Véron-Cetty & Véron (1993). The presence of both quasar and stellar spectral features in PKS 2135-20 suggests that PKS 2135-20 is a radio-loud example of a post-starburst quasar (e.g. Brotherton et al. 1999).

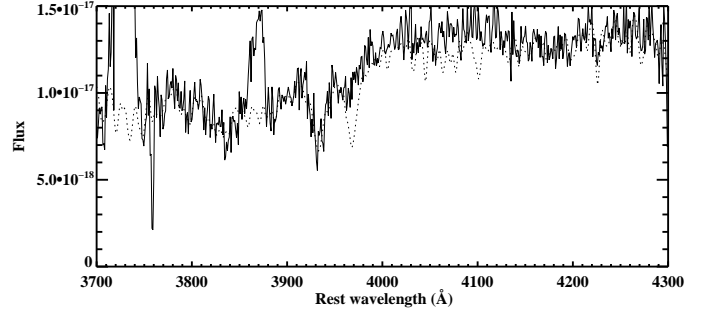
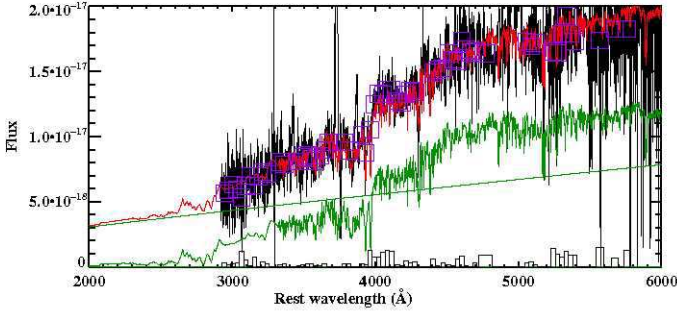
Our new VLT spectrum of PKS 2135-20 is consistent with the detection of broad permitted lines – see Figure 8 for a detailed look at the features in the UV. We therefore confirm the classification of this object as a BLRG or quasar. Given the detection of the broad lines it is likely that a significant power-law component is required. However, it is not possible to model the SED solely with an OSP and a power-law ( $\chi^2_{\text{red}} \sim 2$ ). Hence, we have also attempted to model the SED including a YSP component, consistent with the presence of the higher order Balmer lines in absorption and a significant Balmer break (see Figure 4). In addition, because PKS 2135-20 has one of the highest redshifts in the sample, and we observe down to  $\sim 2300$ Å in the rest frame, we have also investigated the effects of different reddening laws on the YSP.

Figure 3 shows the  $\chi^2_{\text{red}}$  space for three component (OSP, YSP and power-law) models. Consistent with the results for the other sources studied in this paper, a three component model provides a large range of viable fits to the SED. For PKS 2135-20, a clear minimum ( $\chi^2_{\text{red}} \sim 0.45$ ) is observed for YSPs with age  $\sim 0.2$ -0.3 Gyr and reddening  $E(B-V) \sim 0.1$ -0.5.

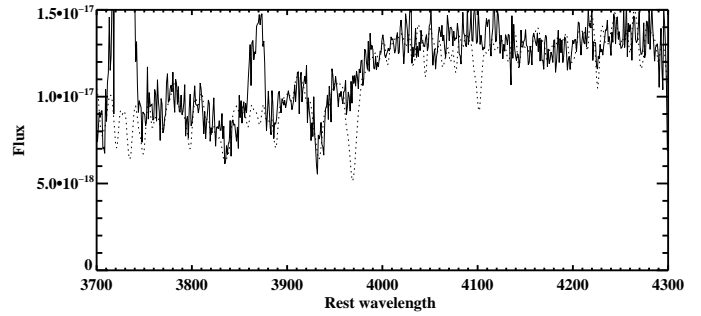
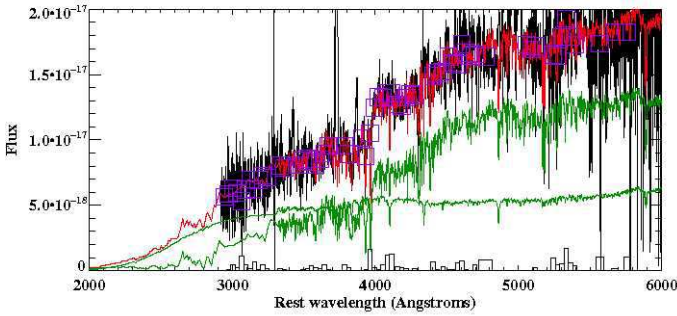
Due to the strong power-law-like continuum shape and broad emission lines, it is difficult to distinguish between the models using the stellar absorption lines – the CaII K and the G-band are relatively weak. A few of the higher order Balmer lines are visible around 3800Å but these appear to be fitted well by all of the models. A possible discriminator could be the continuum shape between  $\sim 3800$ Å and  $\sim 4100$ Å – the older age YSPs ( $\gtrsim 0.7$  Gyr) increasingly underpredict this region and the CaII K line, whereas the younger age YSPs (0.04-0.6 Gyr) reproduce this region and CaII K well. For this range of ages of YSP, the models typically comprise: OSP (12.5 Gyr; 0-24%), YSP (0.04-0.6 Gyr,  $E(B-V) \sim 0.2$ -0.5; 45-77%) and power-law ( $\alpha \sim -1.3$  – -1.4; 3-42%) with  $\chi^2_{\text{red}} \sim 0.4$ -0.6. Note, the OSP and YSP contributions decrease with increasing age of the YSP, but the power-law component increases. An example of a model in the best fitting range is shown in Figure 4: 12.5 Gyr OSP (22%) plus 0.2 Gyr YSP ( $E(B-V) = 0.2$ ; 45%) plus power-law ( $\alpha = -1.47$ ; 34%) with  $\chi^2_{\text{red}} = 0.42$ .

As for some of the other sources at high redshift in our sample, we have also attempted to model the SED using a

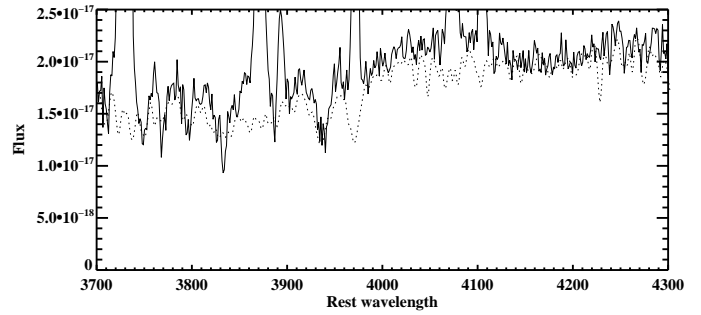
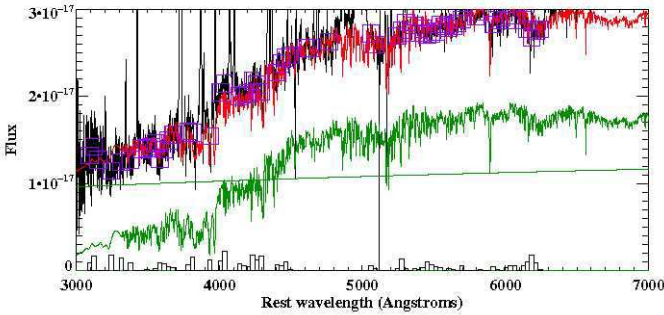
PKS 0409-75: 12.5 Gyr OSP + power law



PKS 0409-75: 12.5 Gyr OSP + 0.02 Gyr YSP ( $E(B-V) = 0.7$ )



PKS 1932-46: 12.5 Gyr OSP + power law



PKS 1932-46: 12.5 Gyr OSP + 0.05 Gyr YSP ( $E(B-V) = 0.4$ ) + power law

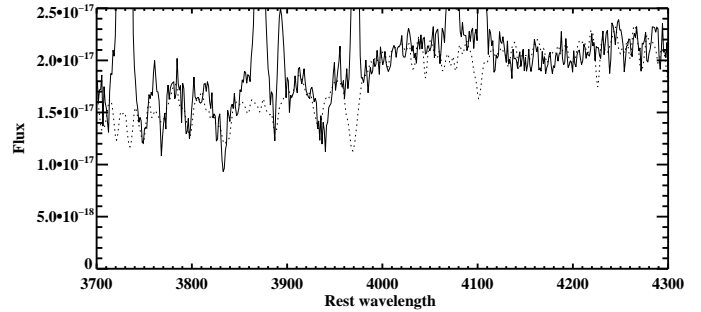
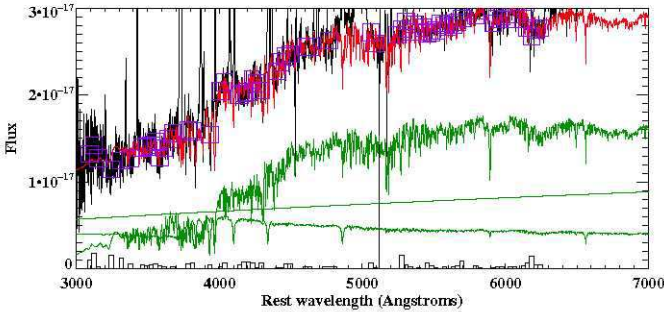


Figure 4. SEDs and detailed fits *continued*

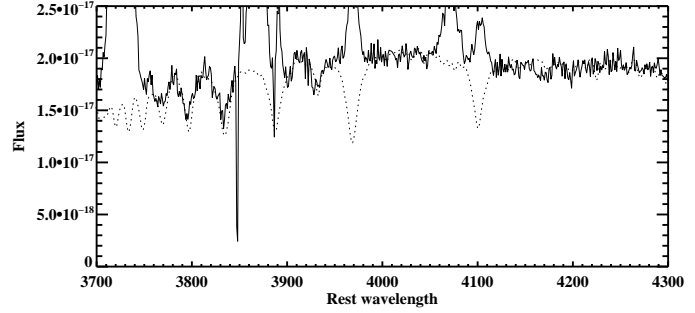
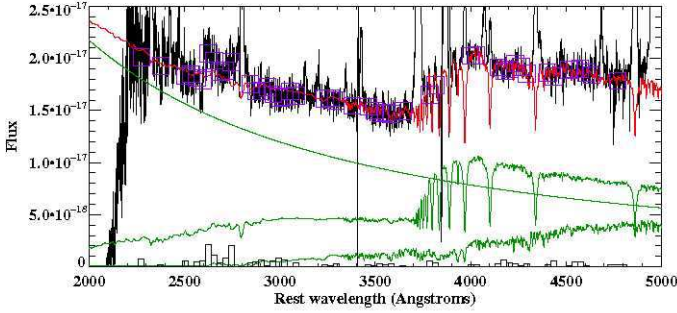
younger OPS with age 7 Gyr — consistent with the age of the Universe at the redshift of the source. This gave similar results to the 12.5 Gyr OSP models – the level, pattern and location of the minimum of the  $\chi^2_{\text{red}}$  space contours are similar, as are the detailed fits.

#### 4.3.12 NGC 612

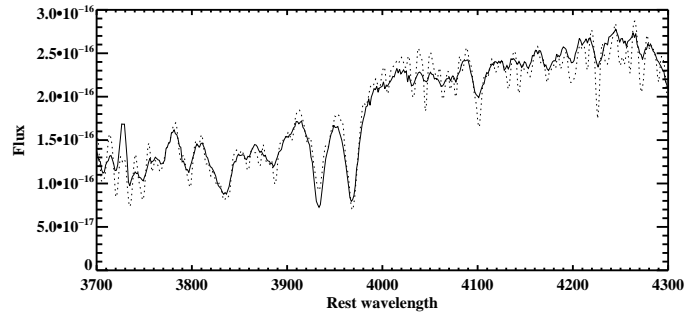
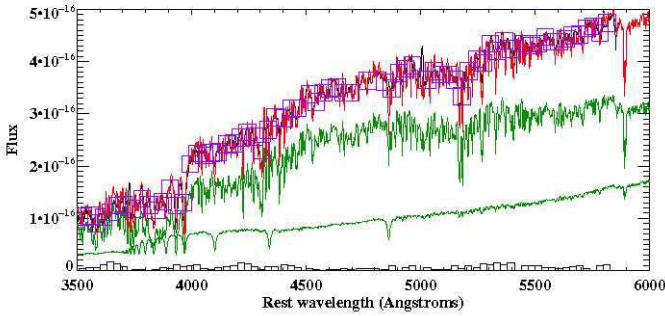
NGC 612 is the nearest radio source in our sample ( $z = 0.030$ ) and, unusually for a powerful radio source, is optically identified with a peculiar lenticular/S0 galaxy with a prominent dust lane and stellar disk (Westerlund & Smith 1966; Ekers et al. 1978). NGC 612 also contains a galaxy-scale disk of neutral hydrogen (HI) gas, which follows the op-



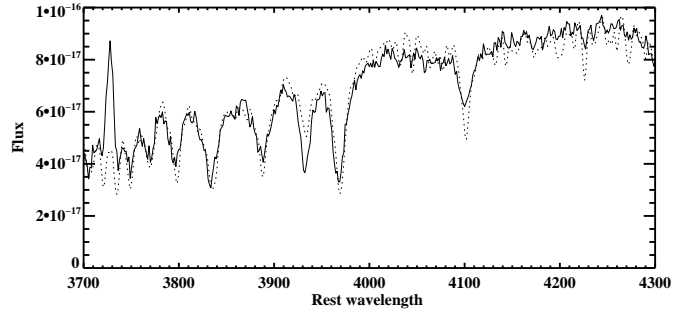
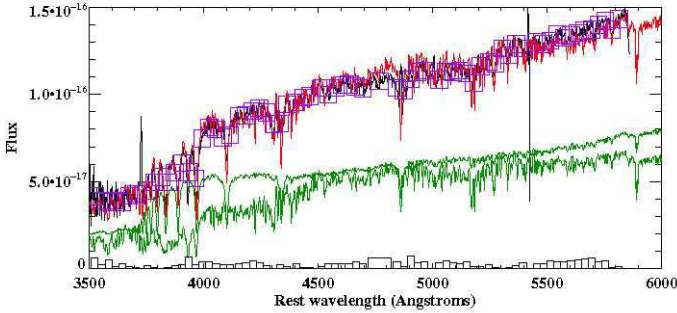
PKS 2135-20: 12.5 Gyr OSP + 0.2 Gyr YSP ( $E(B-V) = 0.2$ ) + power law



NGC 612 (nuc): 12.5 Gyr OSP + 0.05 Gyr YSP ( $E(B-V) = 1.2$ )



NGC 612: (A): 12.5 Gyr OSP + 0.1 Gyr YSP ( $E(B-V) = 0.9$ )



NGC 612: (B): 12.5 Gyr OSP + 0.1 Gyr YSP ( $E(B-V) = 0.6$ )

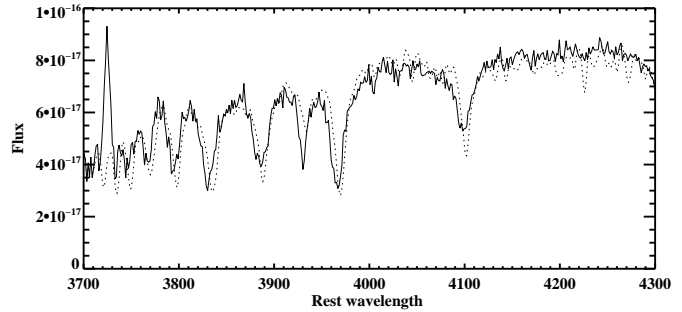
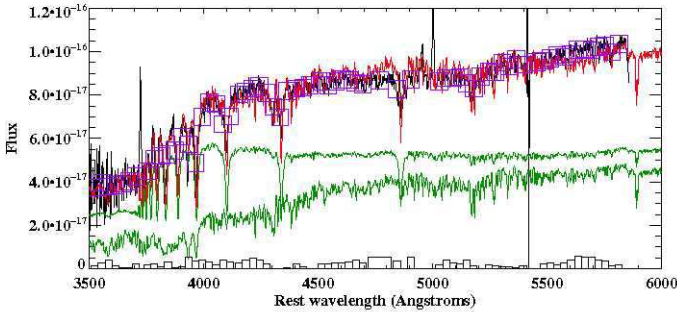
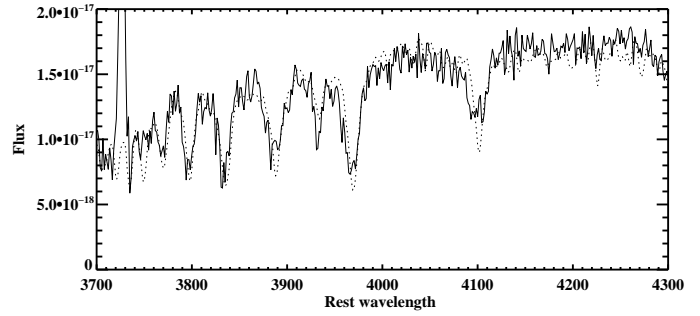
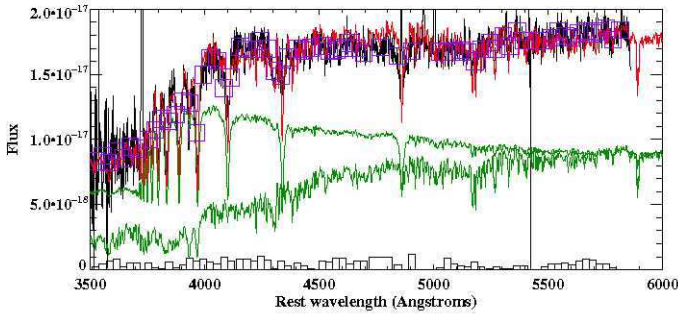
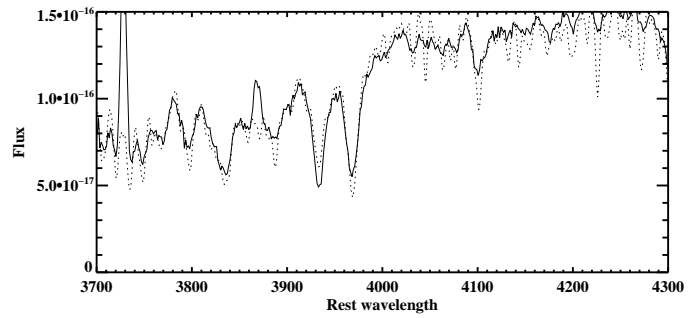
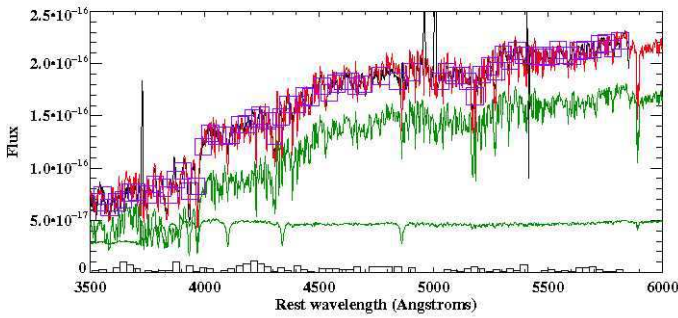
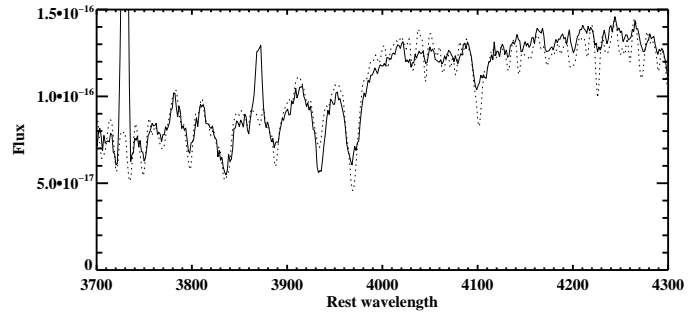
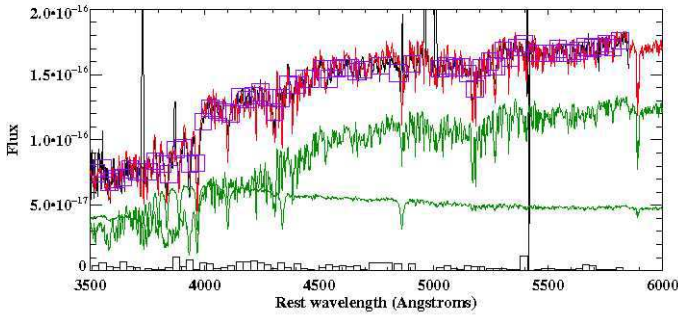
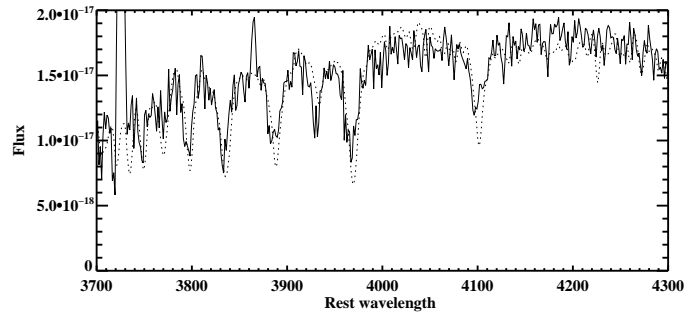
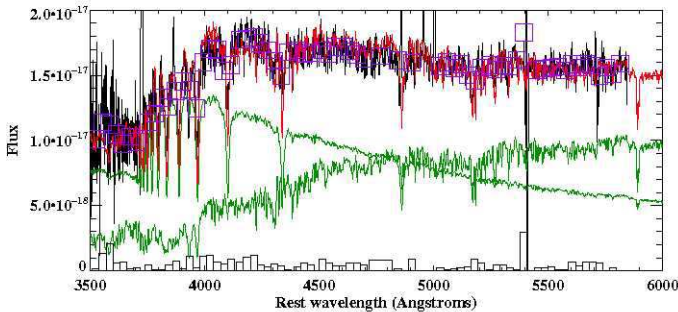


Figure 4. SEDs and detailed fits *continued*

tical disk and dust-lane of the galaxy Emonts 2006; Emonts et al. 2007 in prep). Several authors have noted similarities to Centaurus A (e.g. Westerlund & Smith 1966; Ekers et al. 1978). The double radio source spans  $\sim 14$  arcmin ( $\sim 0.4$  Mpc) and is oriented approximately E-W, perpendicular to the dust lane. Due to its proximity, NGC 612 is well resolved spatially. Line and continuum emission is observed to large

radii, although the emission lines (e.g. [O II], [O III], [N II] and  $H\alpha$ ) are weak (Westerlund & Smith 1966; Goss et al. 1980; Tadhunter et al. 1993). In addition, as well as the usual absorption features associated with an OSP, the higher Balmer lines are detected in absorption (Tadhunter et al. 1993, see also Figure 4), suggesting a significant YSP component. Raimann et al. (2005) have recently modelled the

NGC 612: (C): 12.5 Gyr OSP + 0.1 Gyr YSP ( $E(B-V) = 0.4$ )NGC 612: (D): 12.5 Gyr OSP + 0.05 Gyr YSP ( $E(B-V) = 0.6$ )NGC 612: (E): 12.5 Gyr OSP + 0.05 Gyr YSP ( $E(B-V) = 0.4$ )NGC 612: (F): 12.5 Gyr OSP + 0.1 Gyr YSP ( $E(B-V) = 0.0$ )Figure 4. SEDs and detailed fits *continued*

stellar populations in NGC 612 using five distinct components, finding evidence that  $> 30\%$  of the light in the nuclear and extended apertures is attributable to young stars with age 0.003-1 Gyr with the 1Gyr component being the dominant YSP.

The slit position chosen for the current study was aligned parallel to the large-scale dust lane and stellar disk.

Figure 1 demonstrates that the UV excess extends out to a radius of at least 25 arcsec from the nucleus in both directions. Interestingly, the UV excess *increases* with distance from the nucleus – the nucleus itself has the largest  $D4000$  ratio. This is in contrast to the other spatially resolved sources in the sample which generally have either a constant  $D4000$  ratio across the galaxy or a peak in the UV

**Table 3.** Best fitting models to the galaxy continua. Columns are: (a) aperture (see Figure 1 for sizes and positions); (b) percentage contribution of the subtracted nebular continuum *by flux* in the bin 3540-3640Å (i.e. corresponding to the region of the *maximum* nebular continuum contribution) reddened (where applicable) using the Seaton (1979) reddening law; (c) percentage of OSP (12.5 Gyr); (d) percentage of YSP; (e) age of YSP in Gyr; (f) degree of reddening required for the YSP; (g) percentage of power law component; (h) spectral index of power law; (i) percentage of total stellar mass attributed to the YSP component; (j) best reduced chi squared obtained. \* denotes galaxies best modelled with a different age of OSP: PKS 0039-44 (7 Gyr), PKS 0409-75 (7 Gyr). † *all* ages of YSP give an acceptable fit ( $\chi_{\text{red}}^2$  and absorption lines) but there exists a clearly defined minimum in the  $\chi_{\text{red}}^2$  space – see text.

		Nebular %	Old %	YSP %	YSP age Gyr	E(B-V)	Power law %	Power law $\alpha$	YSP mass %	$\chi_{\text{red}}^2$
(a)	(b)	(c)	(d)	(e)	(f)	(g)	(h)	(i)	(j)	
3C 218	nuc	<1	<b>45</b>	<b>50</b>	<b>0.05</b>	<b>0.4</b>	–	–	<b>4.1</b>	<b>1.2</b>
3C 236	nuc	<1	<b>75-100</b>	<b>10-30</b>	<b>0.04-1.0</b>	<b>1.6-0.6</b>	–	–	<b>20-32</b>	< <b>1.0</b>
		<1	87	–	–	–	12	3.6	–	1.1
3C 285	nuc	1.8	<b>72-68</b>	<b>33-39</b>	<b>0.1-0.5</b>	<b>0.2-0.0</b>	–	–	<b>2.0-2.5</b>	<b>0.7-1.4</b>
3C 321	SE nuc	5.8	<b>15-55</b>	<b>30-60</b>	<b>0.1-1.0</b>	<b>0.3-0.1</b>	<b>10-20</b>	<b>0.0-0.6</b>	<b>1-34</b>	<b>~0.3</b>
	NW nuc	17.7	<b>12-67</b>	<b>25-75</b>	<b>0.1-1.4</b>	<b>0.3-0.1</b>	<b>5-15</b>	<b>-0.5 – 0.8</b>	<b>2-54</b>	<b>0.4-0.5</b>
	mid	0.3	<b>30-50</b>	<b>40-60</b>	<b>0.4-1.0</b>	<b>0.0-0.1</b>	<b>5-8</b>	<b>-1.6 – -1.7</b>	<b>4-15</b>	<b>0.2-0.5</b>
	ext	25.2	<b>20-36</b>	<b>54-72</b>	<b>0.7-1.0</b>	<b>0.0</b>	<b>5-6</b>	<b>-1.2 – -1.3</b>	<b>8-23</b>	<b>0.7-0.9</b>
3C 381	nuc	1.7	<b>80</b>	–	–	–	<b>20</b>	<b>1.65</b>	–	<b>0.9</b>
		1.7	82	17	0.02	1.0	–	–	4	0.9
3C 433	SW nuc	4.5	<b>67-80</b>	<b>30-20</b>	<b>0.03-0.1</b>	<b>0.8-0.4</b>	–	–	<b>5-30</b>	<b>0.6-1.0</b>
		4.5	74	–	–	–	24	1.0	–	1.4
		4.5	70-20	20-70	0.05-1.4†	0.7-0.3 †	5-20	$\gtrsim 0.0$	6-80	$\lesssim 0.6$
	NE nuc	4.5	<b>65-95</b>	<b>5-30</b>	<b>0.03-1.4</b>	<b>0.3-0.9</b>	–	–	<b>1-15</b>	<b>0.5-0.9</b>
		4.5	100	–	–	–	–	–	–	1.1
		4.5	95-65	4-30	0.03-1.6	0.9-0.3	–	–	1-16	0.5-0.9
	mid	<1	<b>80-95</b>	<b>10-25</b>	<b>0.05-1.0</b>	<b>0.7-0.0</b>	–	–	<b>1-4</b>	<b>0.9-1.1</b>
PKS 0023-26	nuc	22.5	<b>40-54</b>	<b>50-60</b>	<b>0.03-0.05</b>	<b>0.7-0.9</b>	–	–	<b>9-18</b>	<b>0.9-1.1</b>
		22.5	<50	10-60	0.05-1.2	<1.0	<50	$\gtrsim 0.0$	–	0.6-0.9
PKS 0039-44*	nuc	11.7	<b>57</b>	–	–	–	<b>40</b>	<b>-0.5</b>	–	<b>0.4</b>
PKS 0409-75*	nuc	6.0	<b>55-80</b>	<b>45-25</b>	<b>0.01-0.04</b>	<b>0.9-0.5</b>	–	–	<b>9-4</b>	<b>0.8</b>
		6.0	60	–	–	–	45	0.86	–	1.2
PKS 1932-46	nuc	21.9	<b>59</b>	–	–	–	<b>41</b>	<b>0.23</b>	–	<b>0.8</b>
		21.9	0-60	10-80	<i>all</i> †	<i>all</i> †	5-40	>-0.6	<100	0.4-0.8
PKS 2135-20	nuc	13.9	<b>24-0</b>	<b>77-45</b>	<b>0.04-0.6</b>	<b>0.5-0.2</b>	<b>3-42</b>	<b>-4 – -1</b>	<b>16-100</b>	<b>0.4-0.6</b>
NGC 612	nuc	<1	<b>77-73</b>	<b>25-28</b>	<b>0.05-0.1</b>	<b>1.4-1.2</b>	–	–	<b>19-28</b>	<b>0.5-0.3</b>
	A	<1	<b>47-51</b>	<b>56-54</b>	<b>0.05-0.1</b>	<b>0.9-1.0</b>	–	–	<b>27-28</b>	<b>0.5-0.6</b>
	B	<1	<b>30-45</b>	<b>70-60</b>	<b>0.05-0.1</b>	<b>0.8-0.6</b>	–	–	<b>14-29</b>	<b>0.6</b>
	C	<1	<b>30-45</b>	<b>70-60</b>	<b>0.05-0.1</b>	<b>0.6-0.4</b>	–	–	<b>15-7</b>	<b>0.5</b>
	D	<1	<b>70-80</b>	<b>30-23</b>	<b>0.04-0.2</b>	<b>0.8-0.3</b>	–	–	<b>7-2</b>	<b>0.4-0.6</b>
	E	<1	<b>66-69</b>	<b>37-35</b>	<b>0.04-0.05</b>	<b>0.5-0.4</b>	–	–	<b>3-2</b>	<b>0.5-0.4</b>
	F	<1	<b>25-50</b>	<b>75-54</b>	<b>0.05-0.1</b>	<b>0.4-0.0</b>	–	–	<b>10-1</b>	<b>0.5-0.6</b>

excess in the nucleus. In addition to modelling the nuclear aperture, we have also extracted 6 extended bins in the disk of the galaxy. All apertures are highlighted in Figure 1.

**The nucleus.** It is not possible to model the nuclear aperture of NGC 612 with an OSP, with or without an power-law component ( $\chi_{\text{red}}^2 > 2$ ) and so a YSP component is essential to model the SED. Figure 3 shows the  $\chi_{\text{red}}^2$  space for

two component (OSP plus YSP) models. in which the YSP is reddened using both the Seaton (1979) and Calzetti et al. (2000) reddening laws. We find that use of Calzetti et al. (2000) rather than the Seaton (1979) reddening law for the YSP makes little difference to our results (see Section 5.2 therefore for the analysis presented here, we shall focus on the results obtained using the Seaton (1979) law.

Two component fits (OSP plus reddened YSP) provide viable fits for ages 0.1-2.0 Gyr with two distinct minima at  $\sim 0.1$  Gyr ( $E(B-V) \sim 1.2$ ) and  $\sim 0.9$  Gyr ( $E(B-V) \sim 0.6$ ) with  $\chi_{\text{red}}^2 = 0.29$  and  $0.31$  respectively (Figure 3). Hence, as with many of the apertures, it is impossible to distinguish between the models on the basis of the  $\chi_{\text{red}}^2$  to the overall SED alone.

Based on the detailed fits, models including YSPs with ages 0.03-0.1 Gyr ( $E(B-V) \sim 1.4-1.2$ ) provide the best fit to the absorption features and continuum in the range 3700-4300Å, with contributions of 80-75% and 20-28% for the 12.5 Gyr and YSP components respectively. Models including YSPs with ages  $> 0.2$  Gyr tend to either over-estimate the continuum in the region 4000-4100Å and/or over-estimate the strength of the Ca K line, especially as the age of the YSP increases. Figure 4 shows the SED and Balmer line fits for the 12.5 OSP plus 0.05 Gyr YSP with  $E(B-V) = 1.2$  and  $\chi_{\text{red}}^2 = 0.3$ .

The fits were not significantly improved when including a power-law component. This is not surprising given that NGC 612 has no strong evidence for a power law component – the emission lines are weak and previous work has not discovered significant polarised light (optical polarisation  $\lesssim 2\%$ ; Brindle et al. 1990).

**Extended apertures** As discussed above, NGC 612 is spatially well resolved and the UV excess covers the entire spatial extent of the galaxy. Further, given that an AGN component is not likely to be significant in the nuclear regions, it is also logical to assume the extended regions also do not have a power-law component. The analysis therefore focusses on modelling the extended aperture SEDs using a combination of OSP and reddened YSP components.

As in the nuclear aperture, a pure OSP fails to provide an adequate fit to the SED in all of the extended apertures ( $\chi_{\text{red}}^2 > 6$ ) and a YSP component is required. Indeed, including a YSP component significantly improves the fits in all extended apertures – solutions are found with  $\chi_{\text{red}}^2 < 1$ , see Figure 3.

The minimum chi-squared plots for apertures A, B, D and E show two minima at  $\sim 0.05 - 0.1$  Gyr ( $E(B-V) \sim 0.5 - 1.0$ ) and  $\sim 1.0$  Gyr ( $E(B-V) \sim 0.0 - 0.3$ ). However, consistent with fits to the spectra of other objects, the older ages (second minimum) can be ruled out due to the over prediction of the strength of CaII K, and failure to provide an adequate continuum fit in the region around 3700-4300Å. The cases of apertures C and F are more clear-cut in the sense that only models with relatively young ages (0.04 – 0.1 Gyr) and moderate reddening ( $0.1 < E(B-V) < 0.2$ ) provide adequate fits to the SEDs. It is notable, however, that although the YSP models with ages  $\sim 0.04 - 0.1$  provide a good fit to the continuum SEDs and the higher Balmer absorption lines, they significantly underpredict the strength of the CaII K absorption feature in all the extended apertures. One plausible explanation for this is that CaII K absorption due to intervening ISM is important for these apertures. Such an explanation is consistent with the relatively high reddening deduced for the YSP in these extended apertures, as well as the alignment of the slit with the large-scale dust lane.

It is also worth noting that, in apertures C and F, the absorption line profiles are complex and appear to have a split profile. At these positions, there is an enhancement in the continuum brightness on the 2D spectra and, in the case

of aperture C, a ‘blob’ in the galaxy halo. This may be the signature of stellar populations which are offset in velocity e.g. a young star-forming cluster in the halo which is moving differently to the older stars in the galaxy. However, the data presented here have insufficient resolution and S/N to investigate this issue and we have assumed the absorption profiles can be modelled by up to two stellar populations at the same velocity.

**Summary for NGC 612.** The high spatial resolution of the continuum structure in NGC 612 allows us to note some interesting trends in the stellar populations in this radio galaxy: the model fits for all apertures are consistent with a combination of an OSP and a reddened YSP of age  $\sim 0.04 - 0.1$  Gyr, with the contribution of the YSP decreasing towards the nucleus – as expected for an SO galaxy. However, although we cannot absolutely rule out a contribution by an older ( $\sim 1$  Gyr) reddened YSP in the nuclear regions, our spectra are not consistent with the presence of the dominant  $\sim 1$  Gyr unreddened YSP deduced by Raimann et al. (2005).

## 5 DISCUSSION – DETERMINING THE PROPERTIES OF THE YSP IN RADIO GALAXIES

The results presented in this paper provide a good illustration of the challenges faced when determining the properties of the stellar populations in AGN host galaxies. The issues that need to be considered are discussed in the following sections.

### 5.1 AGN-related components.

As stressed in previous studies (e.g. Tadhunter et al. 1996, 2002), AGN continuum and emission line components have a major effect on the the continuum spectra of radio galaxies at optical and UV wavelengths. In the current study, scattered AGN light is important for at least two objects (PKS 0039-44, 3C 321), a further three objects show good evidence for directly transmitted AGN light (PKS 1932-46, PKS 2135-20, 3C 381), and nebular continuum and emission line infilling of absorption lines is important in most objects (see Table 4). To illustrate this point Figure 9 shows an example of the correction for both nebular continuum and the emission line infilling of the higher order Balmer lines in the case of the extended aperture of 3C 321. Not only does the nebular continuum make a large contribution to the UV continuum below the Balmer break in this case ( $\sim 25\%$ ), but infilling of the absorption lines is also important: the higher order Balmer lines (e.g. H9, H10) only become visible in absorption following the subtraction of our nebular model (based on H $\beta$ ). Clearly, failure to take into account the AGN-related components may lead to the wrong solution in terms of modelling the YSP.

### 5.2 Reddening of the YSP.

We often find that YSP models with significant reddening are required in order to obtain good fits to the spectra of

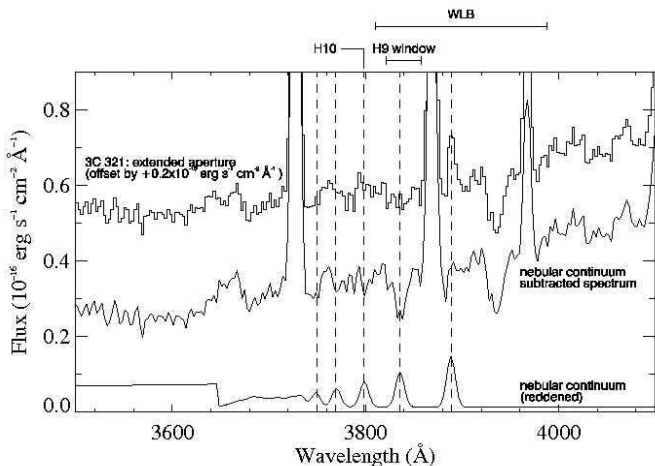


**Figure 9.** The effect of the nebular correction in the extended aperture of 3C 321. The different spectra are labelled in the plot and the dotted lines are to aid the eye for comparisons between the original spectrum, the nebular model and the nebular model subtracted spectrum. In this aperture, the nebular component contributes  $\sim 25\%$  of the flux in the region 3540–3640Å and  $\sim 12\%$  of the flux in the H9 window (3822–3858Å) defined by Raimann et al. (2005). The location of the H9 window and the WLB window (3810–3988Å), both defined by Raimann et al. (2005) and the position of H10 (used by Aretxaga et al. 2001) are marked on the plot.

many of the objects/apertures in our sample. Although the importance of reddening for the YSP has been discounted in some previous studies (e.g. Raimann et al. 2005), the detection of significant reddening in the current work is not surprising given the morphological evidence for dusty circumnuclear environments from HST images of several nearby radio galaxies (e.g. de Koff et al. 2000; Allen et al. 2002; Madrid et al. 2006). It is also notable that, while the reddening is often most important in the circumnuclear regions, it can also be significant in the extended haloes and disks of the galaxies (e.g. NGC 612).

Figure 10 highlights the differences in shape between the Seaton (1979) and Calzetti et al. (2000) reddening laws. At optical wavelengths, the Calzetti et al. (2000) curve rises more steeply towards longer wavelengths than the Seaton (1979) law. This difference in shape causes the changes in the contour plots for NGC 612 (Figure 3) – a steeper reddening law (e.g. Calzetti et al. 2000) will require less reddening in terms of  $E(B-V)$  than a shallower curve (e.g. Seaton 1979) to model the SED with the same age YSP. The difference in the optical wavelength range is subtle and so does not pose a major problem for our results as demonstrated by Figure 3. However, in the UV, the curves are markedly different with a prominent hump in the Seaton (1979) curve not observed in the Calzetti et al. (2000) curve. Hence, the choice of reddening curve requires more careful consideration for spectroscopic studies of higher redshift objects that sample the rest-frame UV.

### 5.3 Uniqueness of solution.

Perhaps the greatest problem faced when modelling the YSP in radio galaxies is the degeneracy in the solutions

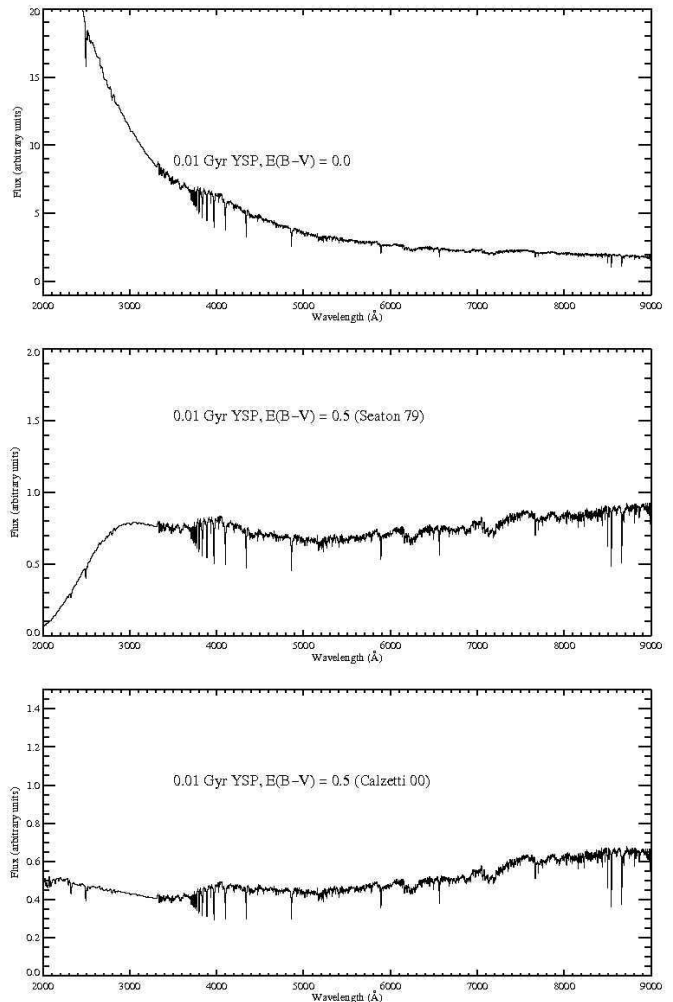


**Figure 10.** Extinction law comparisons. The unreddened 0.01 Gyr YSP from BC03 is plotted (top) and is reddened by  $E(B-V) = 0.5$  using the Seaton (1979) extinction law (middle) and the Calzetti et al. (2000) extinction law (bottom). The extinction laws differ in two respects. First, the re-normalisation factor,  $R$  ( $R = 3.1$  for Seaton (1979),  $R = 4.1$  for Calzetti et al. (2000)) which affects the overall level of the slope and second, the shape in the region 2000–2500Å (the Seaton (1979) has a prominent ‘hump’ at 2175Å, a feature observed in the Galaxy but rarely in extragalactic sources, see Section 5.2) which affects the SED slope in the UV. The Calzetti et al. (2000) curve also has an overall steeper slope towards the red. Hence, it is important to also consider the effect of using a particular reddening law will have on the results when observing sources into the UV.

(see also Tadhunter et al. 2005). Despite the fact that we have adopted the pragmatic approach of modelling the spectra with the minimum number of components necessary (OSP, YSP, power-law), in some cases a wide range of YSP age/reddening combinations can give acceptable fits to the SEDs and absorption features. Unsurprisingly, the degeneracy problem is at its worst for objects in which the YSP component makes a small contribution to the optical/UV continuum relative to the OSP and/or AGN components; the most clear-cut solutions are obtained for the objects/apertures in which the YSP contributes  $>40\%$  of the total flux in the normalising bin. While it is possible to remove some of this

degeneracy through detailed examination of model fits to absorption lines that are not affected by emission line infilling (e.g. CaII K, G-band, MgIb and, in some case, higher order Balmer lines), in a number of cases it has proved necessary to use auxiliary information (e.g. UV polarisation, HST point source, power-law slope) to distinguish between model solutions. Such information is particularly valuable when distinguishing between a very young YSP that is highly reddened, and a scattered or direct AGN component.

It is also important to stress that, because it is not possible to completely eliminate systematic errors in the flux calibration, and the exact choice of bins will also affect the precise  $\chi_{\text{red}}^2$  values of fits, the best solutions numerically (in terms of  $\chi_{\text{red}}^2$  or other numerical measures of goodness of fit), are not necessarily the best solutions in terms of the detailed fits to continuum and absorption lines.

Overall, it is clear that considerable care is required in order to avoid degeneracies in the YSP solutions; the greater the number of stellar components included in the fits the more serious the degeneracy problem is likely to become, especially considering that the different YSP components may be reddened by different amounts. This is why we prefer to model our data with the minimum number of stellar components, rather than assume several components at the outset.

## 6 SUMMARY OF THE MAIN RESULTS

Despite the challenges inherent in studies of this type, we have been able to extract useful information about the detailed properties of the YSP in nine out of the twelve radio galaxies in our sample. For the remaining three galaxies (PKS 0039-44, PKS 1932-46 and 3C 381) we failed to find strong evidence for a YSP based on our spectroscopy, although this does not rule out a contribution from a YSP at some level. Indeed, because of the dominance of the scattered AGN component in PKS 0039-44, and the direct AGN component in PKS 1932-46 and 3C 381, it would be difficult to detect a YSP that contributes as much as  $\sim 20\%$  of the total light, and a greater proportion of the stellar light, in such objects. We now summarise the main results for the YSP in the remaining ten objects for which we have been able to extract useful information.

### 6.1 Spatial extent of the UV excess

A striking aspect of this study is that, for all of the objects that are well-resolved, the UV excesses are spatially extended, covering the full measurable extents of the galaxies. Similar results were found for the four galaxies studied by Tadhunter et al. (2005) & Emonts et al. (2006). Moreover, in all cases in which we have sufficiently high S/N to model the spectra of the off-nuclear emission in detail we find clear evidence for young stellar populations. It is also notable that for the two double nucleus systems in our sample, both of the nuclei in each system show a UV excess. Together, these results suggest that where starbursts occur in radio galaxies, they tend to be galaxy-wide rather than confined to the immediate vicinities of the nuclei hosting the AGN.

### 6.2 Ages of the YSP

The ages of the YSP have the potential to provide key information for understanding the order of events which triggered the AGN in galaxy mergers (see Tadhunter et al. 2005). With regard to the YSP age determination we can divide the current sample into four categories.

(i) **Objects with indeterminate YSP ages: 3C 236, PKS 2135-20, 3C 285.** In these cases the contribution of the YSP is relatively minor over the wavelength range covered by the observations, and, although we believe that there is good evidence for YSPs in these cases, it has not proved possible to determine the YSP ages with any accuracy: all YSP ages ranging from moderately young ( $\sim 0.04 - 0.1$  Gyr) to intermediate ( $\sim 0.5 - 1.0$  Gyr) are possible in these objects.

(ii) **Objects with intermediate YSP ages (0.3 – 3.0 Gyr): 3C 321.** In contrast to some recent studies (e.g. Tadhunter et al. 2005; Emonts et al. 2006; Raimann et al. 2005) we find unequivocal evidence for intermediate age YSPs in only one object: 3C 321. In that case the YSP in the extended apertures (which makes a relatively large contribution to the total optical flux: 40-70%) have age  $\sim 0.7 - 1.0$  Gyr. Although the model results for the other apertures in 3C 321 are less clear-cut, fits to the spectrum of the main (SE) nucleus are also consistent with an intermediate YSP age.

(iii) **Objects with moderately young YSP (0.05 – 0.2 Gyr): 3C 218, NGC 612, 3C 433.** Because of the relatively large proportional contribution of the YSP, weak AGN, and clearly detected Balmer absorption lines, it has proved possible to pin down the YSP ages accurately in 3C 218 and NGC 612. In both of these cases the YSP are moderately young.

(iv) **Objects with very young YSP ( $< 0.05$  Gyr): PKS 0023-26, PKS 0409-75.** A new finding from this study is the existence of a group of powerful radio galaxies with very young, reddened YSP. The clearest case from the SED fits is PKS 0023-26, in which we detect the higher Balmer lines directly in absorption, but, based on consideration of auxiliary data, PKS 0409-75 is also a strong candidate for an object containing a very young YSP. It is not surprising that the young stellar populations in these cases are also heavily reddened, since starbursts are expected to be heavily dust enshrouded in the early stages.

### 6.3 Reddening of the YSP and broad-band colours

A large fraction ( $\sim 70\%$ ) of the objects for which we have good information on the YSP show evidence for significant reddening in their nuclear regions ( $E(B-V) \gtrsim 0.4$ ), and in one case – NGC 612 – we also find evidence for substantial reddening in the off-nuclear regions. Since many studies of AGN host galaxies are based on the broad-band colours, it is interesting to consider the impact that such reddening has on the broad-band continuum colours of the objects in our sample. In Table 4 we show the (B-V) colours derived from our spectra for the objects in our sample along with the three objects in Tadhunter et al. (2005). These colours have been derived by measuring the ratio of the fluxes measured over 500Å bins at the central wavelengths of the B and V filters

**Table 4.**  $B - V$  colours of the nuclei in the rest frame, after correcting for Galactic extinction. To avoid contamination from the emission lines, the colours were measured using the best fitting models to the SED. For comparison, we include the  $B - V$  colour of a 12.5 Gyr stellar population from the Bruzual & Charlot (2003) models.

Object	$B - V$	Object	$B - V$
3C 218	0.67	PKS 0023-26	0.93
3C 236	1.05	PKS 0039-44	0.86
3C 285	0.75	PKS 0409-75	0.84
3C 321	0.71	PKS 1932-46	0.88
3C 381	1.00	PKS 2135-20	0.52
3C 433	0.88	NGC 612	1.03
<hr/>			
12.5 Gyr	0.92		

in the rest frames of the objects. For reference, quiescent elliptical galaxies have  $B - V \sim 0.9$ -1.0.

From Table 4 it is clear that some galaxies have E( $B - V$ ) colours that are significantly bluer than quiescent elliptical galaxies, as expected in the case of major contributions from unreddened YSP and/or scattered AGN components. However, many of the sources have broad-band colours that are similar to, or significant redder than, quiescent elliptical galaxies, despite the clear detection of UV-excesses based on  $4000\text{\AA}$ , break measurements and, in some cases, strong evidence for YSPs from spectral fitting and the detection of Balmer absorption lines. These results serve to demonstrate that considerable caution is required when making conclusions about the stellar populations in AGN host galaxies on the basis of broad-band colours alone.

#### 6.4 The mass contribution of the YSP

Another significant feature of our results is that the YSP typically make up a significant fraction of the total stellar mass in the regions sampled by the spectroscopic slits ( $\sim 1 - 35\%$ ). Note that this is true even for some of the objects in which the measured age of the YSP is relatively young. In such cases the YSP are often heavily reddened, therefore, although the YSP contribute a relatively small fraction of the total light, they can represent a significant fraction of the total stellar mass.

## 7 CONCLUSIONS

We have modelled deep wide spectral coverage data for a sample of 12 powerful radio galaxies with previous evidence for young stellar populations. The results demonstrate the importance of accounting for AGN contamination and reddening when determining the detailed properties of the stellar populations. Moreover, in cases where the YSP makes a relatively small contribution to the optical/UV continuum, it has proved difficult to determine the precise ages of the YSP. We find that the YSP with well-determined properties cover a wide range of post-starburst ages (0.03 – 1.5 Gyr) and reddening ( $0.0 < E(B - V) < 1.5$ ), and account for a significant fraction of the total stellar mass in the regions

covered by our spectra (1 – 50%). The implications of these results for our understanding of the evolutionary status of radio source host galaxies, and the heating mechanism of the warm/cool dust in AGN, will be discussed in forthcoming papers (Tadhunter et al. 2007a,b).

## ACKNOWLEDGEMENTS

JH, KJI & JR acknowledge financial support from PPARC; KAW acknowledges support from the Royal Society. The William Herschel Telescope is operated on the island of La Palma by the Isaac Newton Group in the Spanish Observatorio del Roque de los Muchachos of the Instituto de Astrofísica de Canarias. This research has made use of the NASA/IPAC Extragalactic Database (NED) which is operated by the Jet Propulsion Laboratory, California Institute of Technology, under contract with the National Aeronautics and Space Administration. Based on observations made with ESO Telescopes at the Paranal Observatory under programme ID 71.B-0616(A).

## REFERENCES

- Allen M. G., Sparks W. B., Koekemoer A., Martel A. R., O’Dea C. P., Baum S. A., Chiaberge M., Duccio Macchetto F., Miley G. K., 2002, *ApJS*, 139, 411
- Alvarez H., Aparici J., May J., Navarrete M., 1993, *A&A*, 271, 435
- Aretxaga I., Terlevich E., Terlevich R., Cotter G., Diaz A. I., 2001, *MNRAS*, 325, 636
- Baum S. A., Heckman T. M., Bridle A. H., van Breugel W. J. M., Miley G. K. M., 1988, *ApJS*, 68, 643
- Baum S. A., Heckman T. M., van Breugel W., 1992, *ApJ*, 389, 208
- Black A. R. S., Baum S. A., Leahy J. P., Perley R. A., Riley J. M., Scheuer P. A. G., 1992, *MNRAS*, 256, 186
- Brindle C., Hough J. H., Bailey J. A., Axon D. J., Sparks W. B., 1990, *MNRAS*, 247, 327
- Brotherton M. S., van Breugel W., Stanford S. A., Smith R. J., Boyle B. J., Miller L., Shanks T., Croom S. M., Filippenko A. V., 1999, *ApJ*, 520, L87
- Bruzual A. G., Charlot S., 1993, *ApJ*, 405, 538
- Bruzual A. G., Charlot S., 2003, *MNRAS*, 344, 1000
- Calzetti D., Armus L., Bohlin R. C., Kinney A. L., Koornneef J., Storchi-Bergmann T., 2000, *ApJ*, 533, 682
- Chiaberge M., Capetti A., Celotti A., 1999, *A&A*, 349, 77
- Chiaberge M., Capetti A., Celotti A., 2002, *A&A*, 394, 791
- Cohen M. H., Ohle P. M., Tran H. D., Goodrich R. W., Miller J. S., 1999, *AJ*, 118, 1963
- David L. P., Arnaud K. A., Forman W., Jones C., 1990, *ApJ*, 356, 32
- de Grijp M. H. K., Keel W. C., Miley G. K., Goudfrooij R., Lub J., 1992, *A&A*, 96, 389
- de Koff S., Baum S. A., Sparks W. B., Biretta J., Golombek D., Macchetto F., McCarthy P., Miley G. K., 1996, *ApJS*, 107, 621
- de Koff S., Best P., Baum S. A., Sparks W., Röttgering H., Miley G., Golombek D., Macchetto F., Martel A., 2000, *ApJS*, 129, 33

- de Vaucouleurs G., de Vaucouleurs A., Corwin Jr H. G., Buta R. J., Paturel G., Fouque P., 1991, Catalogue, Third reference catalogue of bright galaxies, version 3.9
- Dennett-Thorpe J., Barthel P. D., van Bemmell I. M., 2000, *A&A*, 364, 501
- di Serego Alighieri S., Danziger I. J., Morganti R., Tadhunter C. N., 1994, *MNRAS*, 269, 998
- Dickson R. D., 1997, PhD thesis, University of Sheffield
- Dickson R. D., Tadhunter C. N., Shaw M., Clark N., Morganti R., 1995, *MNRAS*, 273, 29
- Draper P., Scarrott S., Tadhunter C. N., 1993, *MNRAS*, 262, 1029
- Ekers R. D., Goss W. M., Kotanyi C. G., Skellern D. J., 1978, *A&A*, 69, L21
- Emonts B. C. H., Morganti R., Tadhunter C. N., Holt J and Oosterloo T. A., van der Hulst J. M., Wills K. A., 2006, *A&A*, 454, 125
- Emonts B. H. C., 2006, PhD thesis, University of Groningen
- Eracleous M., Halpen J. P., 2004, *ApJS*, 150, 181
- Filippenko A. V., 1987, in
- González Delgado R. M., Cerviño M., Martins L. P., Leitherer C., Hauschildt P. H., 2005, *MNRAS*, 357, 945
- González Delgado R. M., Leitherer C., Heckman T., 1999, *ApJS*, 125, 489
- Goss W. M., Danziger I. J., Fosbury R. A. E., Boksenburg A., 1980, *MNRAS*, 190, 23
- Grandi S. A., Osterbrock D. E., 1978, *ApJ*, 220, 783
- Hansen L., Jorgensen H. E., Norgaard-Nielsen H. U., 1996, *A&A*, 297, 13
- Heckman T. M., Smith E. P., Baum S. A., van Breugel W. J. M., Miley G. K., D I. G., D B. G., B B., 1986, *ApJ*, 311, 526
- Hill G. J., Goodrich R. W., Depy D. L., 1996, *ApJ*, 462, 163
- Holt J., 2005, PhD thesis, University of Sheffield
- Holt J., Tadhunter C. N., Morganti R., 2003, *MNRAS*, 342, 227
- Holt J., Tadhunter C. N., Morganti R., Bellamy M. J., González Delgado R. M., Tzioumis A., Inskip K. J., 2006, *MNRAS*, 370, 1633
- Kaiser C. R., Schoenmakers A. P., Röttgering H. J. A., 2000, *MNRAS*, 315, 381
- Koski A. T., 1978, *ApJ*, 223, 56
- Lilly S. J., Longair M. S., 1982, *MNRAS*, 199, 1053
- Lilly S. J., Longair M. S., 1984, *MNRAS*, 211, 833
- Lilly S. J., Longair M. S., Miller L., 1985, *MNRAS*, 214, 109
- McCarthy P. J., Spinrad H., van Breugel W., 1995, *ApJS*, 99, 27
- McNamara B. R., 1995, *ApJ*, 443, 77
- Madrid J. P., Chiaberge M., Floyd D., Sparks W. B., Macchetto D., Miley G. K., Axon D., Capetti A., O'Dea C. P., Baum S., Perlman E., Quillen A., 2006, *ApJS*, 164, 307
- Martel A. R., Baum S. A., Sparks W. B., Wyckoff E., Biretta J. A., Golombek D., Macchetto F. D., de Koff S., McCarthy P. J., Kiley G. K., 1999, *ApJS*, 122, 81
- Matthews T. A., Morgan W. W Schmidt M., 1964, *ApJ*, 140, 35
- Melnick J., Gopal-Krishna Terlevich R., 1997, *A&A*, 318, 337
- Morganti R., Killeen N., Tadhunter C. N., 1993, *MNRAS*, 263, 1023
- Morganti R., Oosterloo T. A., Tadhunter C. N., Aiudi R., Jones P., Villar-Martin M., 1999, 140, 355
- Morganti R., Tadhunter C. N., Dickson R., Shaw M., 1997, *A&A*, 326, 130
- O'Dea C. P., Koekemoer A. M., Baum S. A., Sparks W. B., Martel A. R., Allen M. G., Macchetto F. D., 2001, *AJ*, 121, 1915
- Osterbrock D. E., Fulbright J. P., Keane M. J and Trager S. C., 1996, *PASP*, 108, 277
- Prestage R. M., Peacock J. A., 1983, *MNRAS*, 204, 355
- Raimann D., Storchi-Bergmann T., Quintana H., Hunstead R., Wistozki L., 2005, *MNRAS*, 364, 1239
- Riley J. M., Pooley G. G., 1975, *MNRAS*, 80, 105
- Robinson T. G., 2001, PhD thesis, University of Sheffield
- Robinson T. G., Tadhunter C. N., Axon D. J., Robinson A., 2000, *MNRAS*, 317, 922
- Roche N., Eales S. A., 2000, *MNRAS*, 317, 120
- Rudy R. J., Schmidt G. D., Stockman H. S., Moore R. L., 1983, *ApJ*, 271, 59
- Sandage A. R., 1972, *ApJ*, 178, 25
- Schilizzi R. T., W T. W., Conway J. E., Nan R., Miley G. K., Barthel P. D., Normandean M., 2001, *A&A*, 368, 398
- Schlegel D. J., Finkbeiner D. P., Davis M., 1998, *ApJ*, 500, 525
- Seaton M. J., 1979, *MNRAS*, 187, 73P
- Shaw M., Tadhunter C. N., Dickson R., Morganti R., 1995, *MNRAS*, 275, 703
- Simkin S. M., 1979, *ApJ*, 234, 56
- Smith E. P., Heckman T. P., 1989, *ApJ*, 341, 658
- Smith R. J., Hudson M. J., Nelan J. E., Moore S. A. W., Quinney S. J., Wegner G. A., Lucey J. R., Davies R. L., Malecki J. J., Scade D., Suntzeff N. B., 2004, *AJ*, 128, 1558
- Spinrad H., Djorgovski S., Marr J., Aguilar L., 1985, *PASP*, 97, 932
- Tadhunter C. N., Dicken D., Holt J., Inskip K. J., Morganti R., Axon D., Buchanan C., González Delgado R. M., Barthel P., van Bemmell I., 2007, accepted, astro
- Tadhunter C. N., Dickson R., Morganti R., Robinson T. G., Wills K., Villar-Martín M., Hughes M., 2002, *MNRAS*, 330, 977
- Tadhunter C. N., Dickson R. C., Shaw M. A., 1996, *MNRAS*, 281, 591
- Tadhunter C. N., Fosbury R. A. E., Quinn P. J., 1989, *MNRAS*, 24, 225
- Tadhunter C. N., Morganti R., di Serego Alighieri S., Fosbury R. A. E., Danziger I. J., 1993, *MNRAS*, 263, 999
- Tadhunter C. N., Morganti R., Robinson A., Dickson R., Villar-Martín M., Fosbury R. A. E., 1998, *MNRAS*, 298, 1035
- Tadhunter C. N., Robinson T. G., González Delgado R. M., Wills K., Morganti R., 2005, *MNRAS*, 356, 480
- Tran H. D., Cohen M. H., Ogle P. M., Goodrich R. W., di Serego Alighieri S., 1998, *ApJ*, 500, 660
- Tzioumis A., King E., Morganti R., Dallacasa D., Tadhunter C. N., Fanti C., Reynolds J., Jauncey D., Preston R., McCulloch P., Tingay S., Edwards P., Costa M., Jones D., Lovell D., Clay R., Meier D., Murphy D., Gough R., Ferris R., White G., Jones P., 2002, *A&A*, 392, 841
- van Breugel W. J. M., Balick B., Heckman T., Miley G.,



- Kelfand D., 1983, *AJ*, 88, 40
- van Breugel W. J. M., Dey A., 1993, *ApJ*, 414, 563
- Vanden Berk D. E., Richards G. T., Bauer A., Strauss M. A., Schneider D. P., Heckman T. M., York D. G., Hall P. B., Fan X., Knapp G. R., Co-authors ., 2001, *AJ*, 122, 549
- Vernet J., Fosbury R. A. E., Villar-Martín M., Cohen M. H., Cimatti A., di Serego Aligieri S., Goodrich D. W., 2001, *A&A*, 366, 7
- Véron-Cetty M.-P., Véron P., 1993, Scientific report 13, A catalogue of Quasars and Active Galactic Nuclei, 6th Edition. European Southern Observatory
- Villar-Martín M., Tadhunter C. N., Morganti R., Clark N., Kileer N., Axon D., 1998, *A&A*, 332, 479
- Villar-Martín M., Tadhunter C. N., Morganti R., Holt J., 2005, *MNRAS*, in press, astro
- Wall J., Peacock J., 1985, *MNRAS*, 216, 173
- Westerlund B. E., Smith L. F., 1966, *Aust. J. Phys.*, 19, 181
- Wills K. A., Morganti R., Tadhunter C. N., Robinson T. G., Villar-Martín M., 2004, *MNRAS*, 347, 771
- Wills K. A., Tadhunter C. N., Robinson T. G., Morganti R., 2002, *MNRAS*, 333, 221
- Zirbel E. L., Baum S. A., 1998, 114, 177